

1.27 Computational Kinetics: Application to Nuclear Materials

Caroline Toffolon-Masclet, University of Paris-Saclay, Gif-sur-Yvette, France

Aurélien Perron, Lawrence Livermore National Laboratory, Livermore, CA, United States

Benoît Mazères, University of Paris-Saclay, Gif-sur-Yvette, France

Sylvain Dépinoy, PSL Research University, Paris, France

Clara Desgranges, Safran-Tech, Châteaufort, Magny-Les-Hameaux, France

Laure Martinelli, University of Paris-Saclay, Gif-sur-Yvette, France

Daniel Monceau, University of Toulouse, Toulouse Cedex 4, France

Xavier Boulnat, Alexandre Mathevon, and Michel Perez, MATEIS, National Institute of Applied Sciences of Lyon, French National Centre for Scientific Research, University of Lyon, Villeurbanne Cedex, France

© 2020 Elsevier Ltd. All rights reserved.

1.27.1	Introduction	851
1.27.2	Basic Concepts	851
1.27.2.1	Gibbs Energy	851
1.27.2.2	Equilibrium Between Phases	852
1.27.2.3	Driving Forces	852
1.27.2.4	Equations of Diffusion	852
1.27.3	Allotropic Transformations Involving Interfacial Diffusion	853
1.27.3.1	Modeling Interface Motion	853
1.27.3.1.1	DICTRA software	853
1.27.3.1.2	Models based on interface friction	854
1.27.3.1.3	The Gibbs energy minimization (GEM) model	854
1.27.3.1.4	The Ekinox numerical code	854
1.27.3.1.4.1	General description	854
1.27.3.2	High Temperature Oxidation of Zr Alloys	855
1.27.3.2.1	Modeling of high temperature oxidation using Ekinox-Zr numerical code	855
1.27.3.2.2	High temperature oxidation	855
1.27.3.2.3	Dissolution of an inner pre-oxide during high temperature oxidation of Zr alloys	855
1.27.3.2.4	Oxidation of a prior-oxidized cladding	857
1.27.3.3	Ferrite δ Sigma-tisation in 316Nb steels	859
1.27.4	Precipitation	863
1.27.4.1	Classical Nucleation and Growth Theories	864
1.27.4.1.1	Nucleation	864
1.27.4.1.2	Growth	864
1.27.4.1.3	Implementations	865
1.27.4.1.4	Limits of CNGTs	865
1.27.4.2	Precipitation of Oxides in ODS Steels	866
1.27.4.2.1	Modeling homogeneous precipitation of oxides in ODS steels with PreciSo	866
1.27.4.2.1.1	Precipitation of Y_2O_3	867
1.27.4.2.1.2	Precipitation of $Y_2Ti_2O_7$	868
1.27.4.2.1.3	Conclusion on PreciSo modeling	868
1.27.4.2.2	Modeling heterogeneous and multi-components precipitation in ODS steels with MatCalc	869
1.27.4.3	Precipitation of Cu in Fe	869
1.27.4.4	Precipitation of Carbides in Bainitic Steels	871
1.27.4.4.1	Model assumptions	871
1.27.4.4.1.1	Matrix	871
1.27.4.4.1.2	Carbides	872
1.27.4.4.1.3	Nucleation and growth parameters	872
1.27.4.4.2	Comparison with experimental results and discussions	872
1.27.4.4.2.1	Evolution of carbide phase fractions	872
1.27.4.4.2.2	Size evolution of carbides	873

1.27.4.4.2.3	Elements concentration variation in solid solution	873
1.27.4.5	Precipitation of β_{Nb} in Zr Alloys	874
1.27.5	Outlooks	876
Acknowledgments		878
References		878

1.27.1 Introduction

Safe operating of nuclear power plants, as well as the design of new generation ones, require an accurate prediction of parts lifespan. Many of these parts undergo microstructural evolution during their service life (*i.e.*, irradiation, ageing, corrosion...). In spite of heavy experimental plans designed to test microstructural evolutions and associated properties, all parts cannot be investigated.

Modeling is then a key tool to predict these evolutions during service life. Such modeling necessarily combines approaches at different scales: from *ab initio* (see Ref. 1) to macroscopic scale (see Ref. 2), including molecular dynamics (see Refs. 3,4), kinetic Monte-Carlo (see Ref. 5), dislocations dynamics (see Ref. 6) and phase field (see Ref. 7).

This article focuses on microscopic scale (the scale of the microstructure), at which solid-solid diffusive phase transformations (as described in Ref. 8) occur. These transformations involve the migration of an interface, whose velocity is driven by either long range diffusion or local rearrangement of atoms. They are described with a mean field approach.

After a brief presentation of thermo-kinetics basic concepts (Section 1.27.2), a special focus will be put on two particular cases: allotropic transformations (Section 1.27.3) and precipitation (Section 1.27.4), modeled using Classical Nucleation and Growth Theories (CNGTs).

Recent examples of phase transformation kinetics modeled by mean field kinetics approaches will be presented. Steels and Zr alloys are two important materials for nuclear applications undergoing allotropic transformations that drive many of their properties. Oxidation of Zr alloys will be presented in Section 1.27.3.2 and ferrite δ sigmatization causing embrittlement of stainless steel will be detailed in Section 1.27.3.3.

Precipitates are important features of the microstructure because they play a key role in material strengthening. Modeling the precipitation of oxides in Oxide-Dispersion Strengthened (ODS) steels, will be the focus of Section 1.27.4.2. It will be followed by a short example showing the advantages and limitations of CNGTs on the precipitation of Cu in steels that causes embrittlement in steels (Section 1.27.4.3). Then, the precipitation of carbides in steels will be presented in Section 1.27.4.4 as well as the precipitation of β_{Nb} in Zr alloys (Section 1.27.4.5).

An article mostly dedicated to computational thermodynamics on nuclear fuels can be found in the previous edition (see Ref. 9).

This article is based on the knowledge computational thermodynamics (*i.e.*, thermodynamics databases described in Ref. 10).

1.27.2 Basic Concepts

1.27.2.1 Gibbs Energy

The Gibb's energy, or free enthalpy G , is a very important thermodynamic function that will drive almost all transformations of a given system under standard conditions (constant temperature and pressure). It is the sum of two counteracting contributions: the enthalpy H , that tends to maximize the number of bonds and/or level of order, and the entropy S , that tends to maximize the disorder through:

$$G = H - TS \quad (1)$$

where T is the temperature. The differential form of Eq. (1) is given by:

$$dG = Vdp - SdT + \delta Q - TdS + \sum_j \mu_j dn_j \quad (2)$$

where V is the volume, p is the pressure, δQ is the heat exchange, $\mu_j = \partial G / \partial n_j$ is the chemical potential and n is the number of atomic species j .

Under constant temperature and pressure, in a closed system, the variation of Gibb's energy is equal to $\delta Q - TdS$ and the second law of thermodynamics states that $dQ < TdS$ for an irreversible process and $dQ = TdS$ for a reversible process (at equilibrium). This leads to $dG \leq 0$ and means that any transformation would lead to a free enthalpy decrease. This is why Gibbs energy is called a thermodynamic potential. The last consequence is that at equilibrium:

$$dG = 0 \quad (3)$$

1.27.2.2 Equilibrium Between Phases

In a system containing two phases α and β that can exchange atoms of N atomic species, the equilibrium condition (Eq. 3) means that transferring an infinitely small amount of atoms j from one phase to the other does not change the energy. Thus, for each atomic species j :

$$-dn_j \frac{\partial G^\alpha}{\partial n_j^\alpha} + dn_j \frac{\partial G^\beta}{\partial n_j^\beta} = 0 \quad (4)$$

This leads to the well-known rule of equilibrium: at equilibrium, the chemical potential of all elements is the same in all phases:

$$\mu_j^\alpha = \mu_j^\beta \quad (5)$$

However, this rule is not exactly true in all cases. For example, if one phase is a stoichiometric compound (e.g., Y_2O_3), the chemical potential in β phase cannot be defined as above. Let's assume that β phase is a stoichiometric compound of concentration X_j^β , the equilibrium condition means that transferring dn molecules from α to β phase leads to a free enthalpy change of:

$$dG = dn \frac{\partial G^\beta}{\partial n^\beta} - \sum_j^n dn X_j^\beta \mu_j^\alpha = 0 \quad (6)$$

Instead of having N equations for equilibrium (one for each atomic species), there is only one left in the case of a stoichiometric compound.

1.27.2.3 Driving Forces

When equilibrium is not (yet) reached, the driving force Δg is evaluated from the energy change when $dn = \sum_j dn_j$ atoms are transferred from α to β :

$$\Delta g = \frac{dG}{dn} = \sum_{j=1}^N (\mu_j^\beta - \mu_j^\alpha) \frac{dn_j}{dn} \quad (7)$$

In the case of a β stoichiometric compound, the driving force is then:

$$\Delta g = \frac{\partial G^\beta}{\partial n^\beta} - \sum_{j=1}^N X_j^\beta \mu_j^\alpha \quad (8)$$

Combining the last equation with the equilibrium equation (Eq. 6), leads to the expression of the molar driving force for stoichiometric compound:

$$\Delta g = \sum_{j=1}^N [\mu_j^\alpha (X_j^\alpha |_{eq}) - \mu_j^\alpha (X_j^\alpha)] X_j^\beta \quad (9)$$

Chemical potentials can be estimated *via* thermodynamical databases (see Ref. 10) or *via* the published solubility products in the case of precipitates.

1.27.2.4 Equations of Diffusion

Diffusion of atomic species as solute atoms in a phase is generally described by a Fick equation relating the flux to the gradient of volume concentration ∇C_j of atom species j :

$$J_j = -D_j \nabla C_j \quad (10)$$

where D_j is the diffusion coefficient of element j in a given phase. However, things are usually much more complex, *i.e.*, the diffusion coefficient can depend on concentration of j atoms, but also on concentration of all other elements. Therefore, the most general form driving the diffusion of atom species j is rather:

$$J_j = - \sum_{i=1}^N M_{ij}(X_1, \dots, X_N) \nabla \mu_i(X_1, \dots, X_N) \quad (11)$$

where M_{ij} is a mobility matrix. The general form of the diffusion equation (Eq. 11) should be generally preferred to the classical Fick equation (Eq. 10) because it can handle cases where diffusion occurs from lower to higher concentrations, e.g., spinodal decomposition, diffusion through a moving interface between two different phases. However, due to its simple form, (Eq. 10) is rather often used in some simple cases (e.g., dilute phases).

Under the following assumptions: (1) diagonal mobility matrix, (2) ideal solution ($\mu_j = \mu_j^0 + RT \ln X_j$); (3) $D_j = M_j RT v_{at}/X_j$, the general diffusion equation is then equivalent to Fick's equation of diffusion.

1.27.3 Allotropic Transformations Involving Interfacial Diffusion

Some elements exhibit more than one stable form in the solid state. They undergo a so called allotropic transformation that is of great importance in their processing applications. Steels and zirconium alloys are two examples, for which many applications concern the nuclear industry.

Steel, the most used alloy in nuclear power plants, has two allotropic forms: bcc ferrite and fcc austenite. Zirconium alloys, used for fuel cladding due to their corrosion resistance and neutron transparency, exhibit also two allotropic forms: hcp α phase and bcc β phase.

These allotropic forms exhibit extremely different properties in terms of mechanical response, assembly, corrosion resistance and radiation damage resistance.

For both cases, depending on temperature and chemical composition, one form becomes more stable than the other and transformation occurs. It is therefore of prime importance to predict the kinetics and products of this transformation.

1.27.3.1 Modeling Interface Motion

Allotropic phase transformations can be modeled *via* the estimation of transformation rate from the diffusion of alloying elements. Such diffusion-controlled models are based on the numerical solution of Fick's equation (Eq. 11).

The most simple of models are based on the assumption of some kind of equilibrium at the interface. From the knowledge of solute concentration at a α/β interface, and solving Fick's equations for solute fluxes, it is possible to estimate interface velocity through a mass balance:

$$v = \frac{D_i^\beta \nabla C_i^\beta - D_i^\alpha \nabla C_i^\alpha}{C_i^\beta - C_i^\alpha} \quad (12)$$

where C_i and D_i are the solute concentrations and diffusion coefficient of element i at the interface in α or β phase.

Local Equilibrium (LE) is the simplest form of equilibrium that can be applied; chemical potentials of all species are equal at the interface:

$$\mu_i^\alpha = \mu_i^\beta \quad (13)$$

In that case, phase diagram can be used to get equilibrium concentrations C_i and associated operative tie-line. For a system of N components, Eqs. (13) and (12) form a system of $2N$ equations and the concentrations in α and β phase are the $2N$ unknowns. Calculation of interface velocity and solute concentrations profile is not trivial: generally, diffusion equations are solved in an implicit scheme to get solute fluxes and interface velocity is calculated from Eqs. (13) and (12). Numerical schemes sometimes suffer from uncertainties and mass balance is not always fulfilled.

In some cases, one element is much faster than others (*e.g.*, C in steels), leading to some kind of particular "dynamic" equilibrium: if slow elements are considered infinitely slow (compared to the fast one), Eqs. (13) and (12) are solved for only the fast element (all other elements do not move): this is called para-equilibrium (PE). In intermediate cases, depending on the bulk composition and the transformation, either Local Equilibrium with Partitioning (LEP) or Local Equilibrium with Negligible Partitioning (LENP) occur (see Ref. 11).

These kind of approaches have been successfully used to model $\gamma \leftrightarrow \alpha$ transformations in steels.¹¹⁻¹⁶

The diffusion module of ThermoCalc (DICTRA) is the most widely used software for modeling phase transformations. It is based on CALPHAD (Computer Coupling of Phase Diagrams and Thermochemistry) formalism¹⁷ and will be presented in the next section.

1.27.3.1.1 DICTRA software

In DICTRA,¹⁸ diffusion is treated with the generalized Fick's equation connecting solute fluxes J_i with chemical potential gradients of all present chemical species:

$$J_i = \sum_j L_{ij} \nabla \mu_j \quad (14)$$

Mobilities L_{ij} are stored in a mobility database. Associated with equilibrium conditions (Eq. 13) and solute flux balance at the interface (Eq. 12), the diffusion equation (Eq. 16) is solved on a grid to predict the interface motion.¹⁹ Several phases (and associated interfaces) can be accounted for (*e.g.*, cementite/austenite/ferrite) and the one-dimensional grid can be adapted to account for planar, spherical or cylindrical symmetry.

DICTRA is based on the assumption that some kind of equilibrium apply at the interface.¹⁸ Unfortunately, this approach cannot reproduce kinetics that deviate from these equilibrium (*i.e.*, transition from para to local equilibrium) and solute flux balance at the interface often leads to numerical issues.¹⁶ For more general cases, other kinds of models are used and will be presented in the next section.

1.27.3.1.2 Models based on interface friction

Mixed-mode models simplify the numerical resolution of the problem by simulating only carbon diffusion but introduce an interface mobility that controls the transformation kinetics. This approach makes it possible to reproduce experimental kinetics,^{15,20-23} but the mobility applied to take into account the interaction of other elements has no physical meaning, limiting thus predictive capacities of such models.

Another family of models assume a quasi-permanent regime at the interface, where the transformation kinetics is driven by the balance between energy dissipation and driving force.^{24,25}

Chen and Perevoshchikova^{26,27} proposed a complete 2D-Phase Field (PF) model to describe the austenite formation during a heating within a ferrite-pearlite matrix. This study is based on a Mixed-mode model including solute drag to take into account the slow partitioning of the substitutional elements. The PF approach is nevertheless based on a mathematical approach that aims to smooth interface and interpolate the properties of each phase within the interface, posing the problem of the real vs modeled interface characteristic size.

1.27.3.1.3 The Gibbs energy minimization (GEM) model

A model based on Gibbs Energy Minimization (GEM) has been recently developed to predict $\gamma \leftrightarrow \alpha$ kinetics in complex alloys.²⁸ For each diffusing element, a unique diffusion profile (including the 2 phases) is computed. The interface is described using chemical potentials driving the thermodynamics of the system. Interface motion and solute fluxes are treated in a simple framework, allowing to predict the kinetics of phase transformations in many cases without any fitting parameters.

The chemical energy of the whole system is the sum of the energy of each element. It is assumed here that the energy of a multi-component system (e.g., FeXY) is the linear combination of the energy of binary systems (FeX + FeY) composing the multi-component system. This hypothesis leads to the simple expression for the Gibbs energy:

$$G = \mu_{\text{Fe}}^0 + \sum_i (\mu_{\text{Fe}}^B(X_i) \cdot (1 - X_i) + \mu_i^B(X_i) \cdot X_i - \mu_{\text{Fe}}^0) \quad (15)$$

where μ_{Fe}^0 is the chemical potential of pure iron, $\mu_{\text{Fe}}^B(X_i)$ and $\mu_i^B(X_i)$ are the chemical potentials of iron and element i in a binary Fe/ i system of composition X_i .

With such an approach, the energy of a multi-component system containing n elements only requires the knowledge of n binary databases, that can be calculated from any database.

The equation of diffusion controlling the profiles of each chemical elements in 1D is given by²⁵:

$$\frac{\partial}{\partial x} \left(D \frac{\partial C_i}{\partial x} + \frac{C_i D_i}{RT} \frac{\partial E_i}{\partial x} \right) = \frac{\partial C_i}{\partial t} \quad (16)$$

where C is the concentration, T is the temperature, x is the distance, R is the ideal gas constant, D is the diffusion coefficient, E is the difference in standard chemical potential of element i in α and γ for pure iron.

The interface displacement is based on Gibbs Energy Minimization (GEM) with respect to the interface position. At each timestep, the interface is moved to a position that fulfills:

$$\frac{\partial G}{\partial x_i} = 0 \quad (17)$$

where x_i is the interface position. Time and space steps have been optimized in order to obtain a stable solution (independent of time and space steps).

1.27.3.1.4 The Ekinox numerical code

Ekinox-Zr is a numerical tool dedicated to the modeling of high temperature oxidation of Zr alloys. It is able to forecast the kinetic growth of $\alpha_{\text{Zr(O)}}$ phase and the oxygen concentration profiles within β_{Zr} phase. This is an adaptation of the Ekinox numerical code,²⁹ originally developed for Ni alloys.³⁰

1.27.3.1.4.1 General description

The adaptation of this code for Zr alloys consisted in considering a non-zero O solubility inside the oxide interface. This led to the addition of a substrate and adding a third interface α/β within the substrate. The oxide growth and the α phase growth are treated as a 1-Dimension (1-D) planar geometry diffusion problem with fixed conditions at mobile interfaces. The following hypotheses are required:

- (1) The system is constituted by three distinct phases forming three adjacent layers: oxide, α phase, β phase;
- (2) The only diffusing component is oxygen;
- (3) Inside the oxide, oxygen diffuses across the oxide layer via the anionic vacancies. Inside both α_{Zr} and β_{Zr} phases, the oxygen diffusion takes place via an interstitial mechanism;
- (4) Only volume diffusion is considered;
- (5) Local thermodynamic equilibrium conditions are assumed at all interfaces;
- (6) In each phase, the oxygen diffusion coefficient is independent of the local concentration of oxygen.

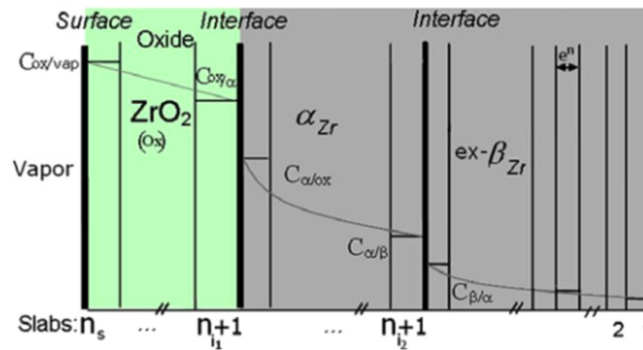


Fig. 1 Schematic representation of the concentration profile. From Corvalan-Moya, C., Desgranges, C., Toffolon-Masclat, C., Servant, C., Brachet, J.-C., 2010. Numerical modeling of oxygen diffusion in the wall thickness of low-tin zircaloy-4 fuel cladding tube during high temperature (1100–1250°C) steam oxidation. *J. Nucl. Mater.* 400 (3), 196–204.

The evolution of the concentration profiles and the interface motion are calculated solving the Fick's equations for oxygen with fixed equilibrium concentration conditions at moving boundaries and considering the oxygen mass balance at the different interfaces. The set of differential equations is solved using a numerical time integration based on explicit finite difference and with an adequate numerical algorithm to tackle the moving interface boundaries issue. The substrate is divided into n_s layers of equal initial thicknesses (Fig. 1). Two sublattices are considered in the oxide: one for the cations and the other one for anions, whereas only one lattice is considered in the metal. This le . Each sub-lattice is filled either by the corresponding chemical species k (metal, oxygen) or by the corresponding vacancies V_k .

Finally, in order to calculate the equilibrium concentrations at each interface, Ekinox-Zr has been linked to the Zircobase thermodynamic database³¹ using the TQ Interface.

1.27.3.2 High Temperature Oxidation of Zr Alloys

1.27.3.2.1 Modeling of high temperature oxidation using Ekinox-Zr numerical code

Zr base alloys are used as nuclear fuel cladding tubes in Pressurized Water Reactors (PWR). Due to the pressurized water environment inside the reactor core, the following reaction takes place at the surface of the cladding: $Zr + 2H_2O \rightarrow ZrO_2 + 2H_2$.

Thus, in normal operating conditions, a ZrO_2 layer forms on the outer part of the cladding with negligible oxygen diffusion inside the oxide interface. This leads to a complex microstructure, constituted, once quenched, by three phases ZrO_2 , $\alpha_{Zr(O)}$ and prior β_{Zr} .³² This microstructure will strongly impact the residual mechanical properties of the High Temperature (HT) oxidized cladding materials: indeed, ZrO_2 and $\alpha_{Zr(O)}$ are brittle. The only remaining ductility at Room Temperature (RT) is found in the prior- β_{Zr} inner layer. However, it has been demonstrated by Brachet *et al.*,³³ from room temperature (RT) impact test data, that the post-quench (PQ) ductile-to-brittle transition within the prior- β layer occurs for a critical oxygen concentration equal to 0.4 wt% (Fig. 2). Three different kinds of simulations will be presented afterwards: high temperature oxidation, dissolution of a pre-existing ZrO_2 layer in a neutral environment and both dissolution and oxidation in the case of a high temperature oxidation of a pre-oxidized cladding.

1.27.3.2.2 High temperature oxidation

Calculated oxygen concentration profiles have been determined for Zircaloy-4 alloys oxidized different times at 1100°C. Zircaloy-4 are typical industrial alloys used as nuclear fuel cladding tubes in PWR. They contain reduced amounts of Sn, Fe, Cr and O. The results have been compared to experimental results obtained by electron microprobe analysis measurements. Calculated and experimental results show a good agreement except for the longest annealing time, 1429 s. For that specific time, $\alpha_{Zr(O)}$ incursions are observed inside prior- β_{Zr} layer due to O saturation of the β phase (Fig. 3).

1.27.3.2.3 Dissolution of an inner pre-oxide during high temperature oxidation of Zr alloys

This example is treated in the framework of hypothetical Loss-of-Coolant-Accident (LOCA) studies. In service conditions, Zr fuel cladding tubes are in contact with the water of the primary circuit at temperatures close to 320°C, leading to the formation of a zirconia layer on the external surface of the tubes but with negligible oxygen diffusion within the α_{Zr} substrate. For high burn-up fuel, formation of a 10–15 μm thick zirconia layer occurs at the inner surface due to the pellet-clad chemical interaction. When a hypothetical LOCA scenario occurs, the cladding can reach temperatures up to 1200°C during a few minutes. Such transient induces an accelerated oxidation of the outer clad surface due to the steam environment. At these high temperatures, it has to be

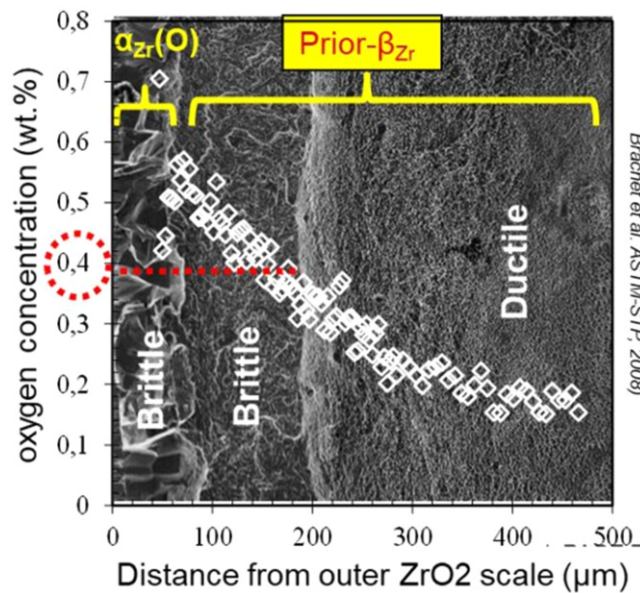


Fig. 2 Fractograph of an impact tested Zircaloy-4 sample at 20°C and associated oxygen diffusion profile within prior- β after steam oxidation for 120 s at 1250°C and quenching. From Brachet, J.-C., Vandenberghe, V., Portier, L., *et al.*, 2008. Hydrogen content, preoxidation, and cooling scenario effects on post-quench microstructure and mechanical properties of zircaloy-4 and m5 alloys in LOCA conditions. *J. ASTM Int.* 5 (5), 28.

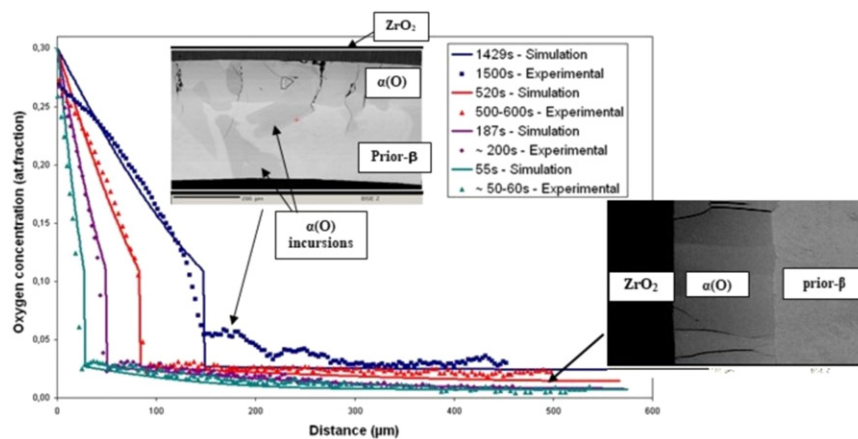


Fig. 3 Comparison between experimental (data from electron microprobe analysis) and calculated O concentration profiles in Zircaloy-4 alloy after oxidation at 1100°C for different times. From Toffolon-Masclat, C., Desgranges, C., Corvalan-Moya, C., Brachet, J.-C., 2011. Simulation of the $\beta \rightarrow \alpha(O)$ phase transformation due to oxygen diffusion during high temperature oxidation of zirconium alloys. *Solid State Phenom.* 172–174, 652–657.

mentioned that, part of the oxygen reacting with the outer clad surface diffuses into the sub-oxide β_{Zr} , inducing the formation of an oxygen stabilized $\alpha_{Zr(O)}$ sub-oxide layer. Thus, the behavior of a pre-existing zirconia layer is peculiar and has been studied experimentally by different authors.^{32,35,36} Indeed, during the first seconds of the treatment, one can notice a reduction of the layer of prior-oxide and the intermediary growth of a $\alpha_{Zr(O)}$ phase. Then, depending on the surrounding atmosphere, oxidation (outer surface) or vacuum (inner surface), and on the initial thickness of the pre-oxide layer, the microstructural evolution is quite different, depending upon the balance of the fluxes at the different interfaces (β_{Zr}/α_{Zr} , α_{Zr}/oxide). In this example, the sequence for a pre-oxidized sample under secondary vacuum has been reproduced by DICTRA calculations. In this case, the zirconia layer completely vanishes in favor of a α_{Zr} phase enriched in oxygen. Then, depending on the time and/or the amount of oxygen inside the system, $\alpha_{Zr(O)}$ phase can also disappear or remain. Four pre-oxide thicknesses have been tested: 5, 15, 25 and 35 μm . For the calculations, three regions have been considered: the first one containing the oxide ($\text{ZrO}_2\text{-MONO}$ phase), at constant oxygen composition, the second one 0.5 μm of $\alpha_{Zr(O)}$ (HCP_A3 phase) with an oxygen composition gradient and the last one, β_{Zr} (BCC_A2 phase), with a constant oxygen layer composition. Indeed, at the beginning of the calculation, it appeared necessary to take into account a very thin intermediate layer, containing $\alpha_{Zr(O)}$ phase in order to ensure the growth of this phase. The results

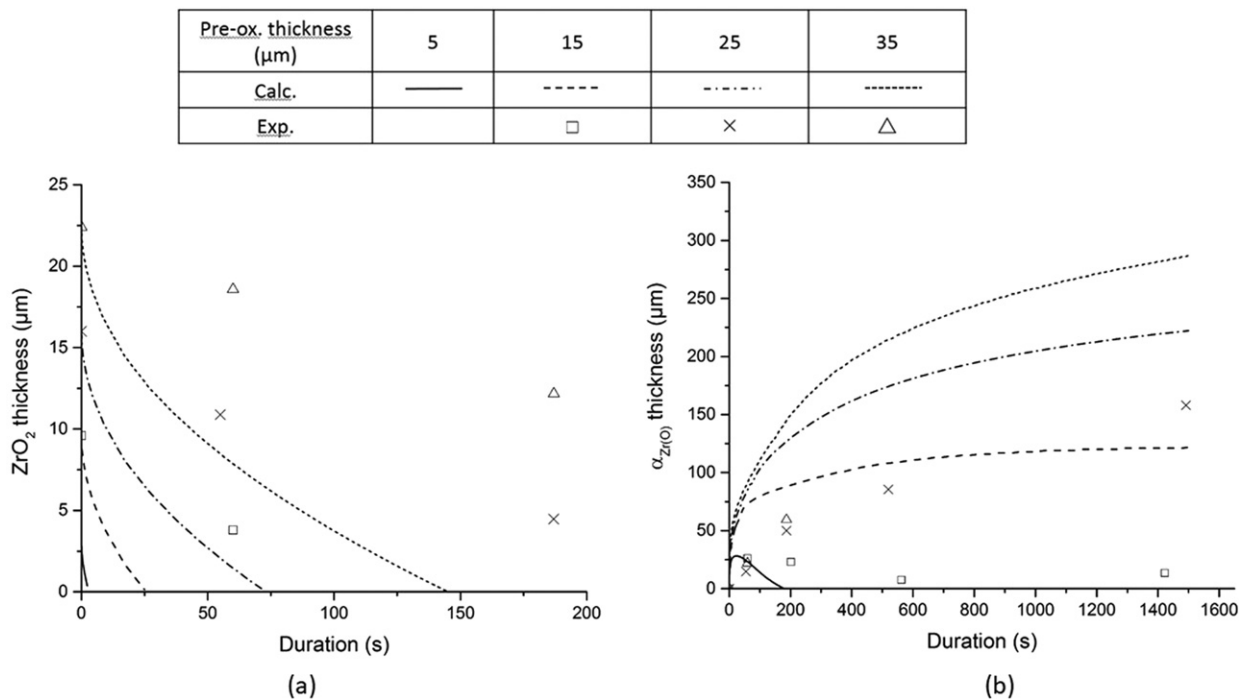


Fig. 4 Variation of $\alpha_{\text{Zr(O)}}$ and oxide thickness as a function of time of isothermal treatment at 1200°C determined by DICTRA calculations for different pre-oxide thicknesses.

obtained are presented in **Fig. 4** showing that, for a 5 μm pre-oxide layer thickness, the oxide and $\alpha_{\text{Zr(O)}}$ completely disappear after, respectively 3 s and 180 s, consistently with some available experimental data.³² On the contrary, for a 25 μm pre-oxide layer thickness, only the oxide disappears after 73 s, two phases $\alpha_{\text{Zr(O)}}$ and β_{Zr} remain at the end of the calculation.

Thus, depending on the time and/or the thickness of the pre-oxide layer, the actual oxygen gradients on both sides of the different interfaces induce their movement. For a pre-oxide layer thickness inferior to 7 μm , first $\alpha_{\text{Zr(O)}}$ grows at the expense of ZrO_2 and β_{Zr} , until the reversing of the oxygen diffusion fluxes across α/β interface leading to the disappearance of $\alpha_{\text{Zr(O)}}$.

In the case of a pre-oxide layer higher than 25 μm , after the disappearance of the oxide layer, there is no reversing of the oxygen diffusion fluxes at α/β interface leading to a stability of both $\alpha_{\text{Zr(O)}}$ and β_{Zr} .

1.27.3.2.4 Oxidation of a prior-oxidized cladding³⁷

It has been demonstrated by different authors^{33,38} that for reduced oxidation times, typically a few tens of seconds, the weight gain of a cladding prior-oxidized at low temperature is inferior to the one of a non-prior-oxidized cladding: indeed, the formation of a new oxide at high temperature is delayed in the case of a prior-oxidized alloy. Yet, the “post-quench” mechanical properties of these prior-oxidized alloys are not improved. Thus, in order to understand the mechanisms occurring at high temperature, several studies have been conducted.^{32,35} These experiments were performed on cladding tubes prior-oxidized at low temperature, and then oxidized under vapor at high temperature. The results show a peculiar behavior: from a given thickness of prior-oxide layer, a reduction is observed during the first seconds at high temperature prior to the regrowth of a fresh oxide. This initial reduction of the thickness of prior-oxide can be explained by the oxygen flux-balance at the oxide interface. This le/oxide interface. During the first seconds of high temperature oxidation, considering the elevated solubility of oxygen in $\alpha_{\text{Zr(O)}}$ phase at these temperatures, the activity gradient of oxygen in the $\alpha_{\text{Zr(O)}}$ layer is high, whereas the oxygen activity gradient is rather low in the thick of prior-oxide. The inward flux of oxygen in the oxide is lower than the inward flux in the $\alpha_{\text{Zr(O)}}$ phase. The balance of the fluxes at the metal/oxide interface leads to the reduction of the prior-oxide despite the oxidizing atmosphere. At a certain time, the flux of oxygen in the $\alpha_{\text{Zr(O)}}$ layer decreases with its thickening, whereas the inward flux of oxygen in the oxide layer increases with the reduction of its thickness. Hence, the balance of the fluxes of oxygen at the metal/oxide interface reverses and the new oxide starts to grow. In this framework, the Ekinox-Zr numerical code has been used in order to understand and quantify the effect of a prior-oxide layer on the oxidation kinetic of Zr alloys at high temperature. It has been necessary to adapt the code by introducing new layers. Hence, several configurations have been tested, they can be found in Ref. 37. We'll present hereafter the results obtained with the most relevant one. Hence, differentiating two ZrO_2 layers, one formed at low temperature and the second at high temperature, and two $\alpha_{\text{Zr(O)}}$ layers, one formed by dissolution of the oxide and the second by oxidation/growth on β_{Zr} , considering the strong differences among their diffusion properties. One of the main results concerns the reduction/re-growth occurrence: the calculations show that it depends on the thickness of the prior-oxide. For instance, growth kinetics of oxide layers in Zy-4 alloys have been calculated at 1200°C, using Ekinox-Zr, considering different thicknesses of prior-oxide (**Fig. 5**).

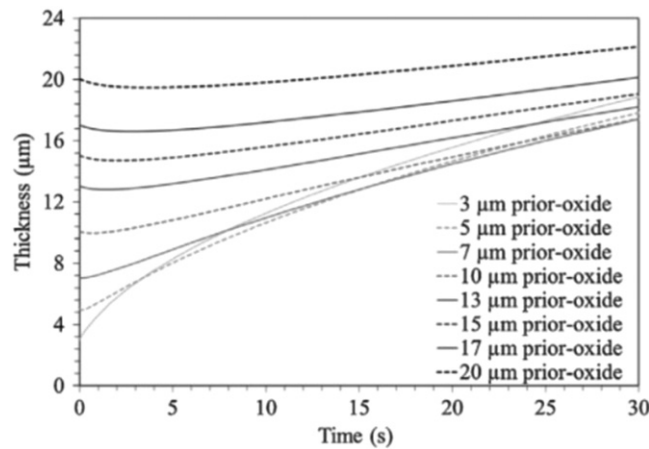


Fig. 5 Calculated growth kinetics of oxide at 1200°C for samples of Zircaloy-4 with different thicknesses of prior-oxide. From Mazères, B., Desgranges, C., Toffolon-Masclét, C., Monceau, D., 2016. Experimental study and numerical simulation of high temperature (1100–1250°C) oxidation of prior-oxidized zirconium alloy. *Corros. Sci.* 103, 10–19.

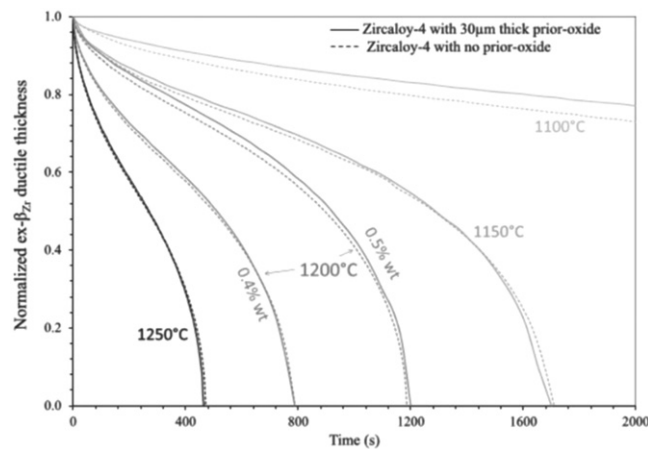


Fig. 6 Variation of the remaining prior- β_{Zr} layer thickness containing less than 0.4%wt. of oxygen (and 0.5 wt% for 1200°C) as a function of time for different temperatures of the high dwell in LOCA conditions. Calculations are made for samples of Zircaloy-4 oxidized on a single face, with and without prior-oxide formed at low temperature during in service conditions. The remaining thickness of the prior- β_{Zr} phase is normalized to the initial thickness (before the high temperature dwell) of β_{Zr} phase. From Mazères, B., Desgranges, C., Toffolon-Masclét, C., Monceau, D., 2016. Experimental study and numerical simulation of high temperature (1100–1250°C) oxidation of prior-oxidized zirconium alloy. *Corros. Sci.* 103, 10–19.

Hence, these calculations demonstrate that at 1200°C, the reduction/re-growth phenomenon is only observed for prior-oxide thicknesses superior to 10 μm . For lower pre-oxide thicknesses, the flux of oxygen in the low temperature oxide layer remains higher than the flux of oxygen in the $\alpha_{Zr(O)}$ layer leading to no decrease of the low temperature oxide layer thickness. The last example deals with the evaluation of the effect of prior-oxides on the ingress of oxygen and their possible influence on the residual ductility of fuel claddings after a LOCA. Calculations have been made considering Zircaloy-4 fuel cladding tube with a 570 μm initial wall-thickness. The initial thickness of the β_{Zr} phase differs between samples with or without prior-oxide layer, thus the evolution of the thickness of the ductile layer of prior- β_{Zr} phase, that is containing less than 0.4 wt% of oxygen, normalized to the initial (*i.e.*, before oxidation at high temperature) thickness of the β_{Zr} layer for each case. The results of the calculations are presented in Fig. 6 showing comparisons for oxidation performed at 1100, 1150, 1200 and 1250°C for as-received and prior-oxidized (30 μm of prior-oxide) samples of Zircaloy-4. These calculations show that the evolution of the prior- β_{Zr} layer is highly influenced by the temperature of oxidation. They also allow to conclude on the consequences of prior-oxidation for various oxidation temperatures and prior-oxide thicknesses. Hence, post-quench ductility of prior-oxidized samples oxidized at temperatures ranging from 1100°C to 1250°C is quite similar to that of as-received samples oxidized under similar conditions. Ekinox-Zr calculations confirm the non protective effect of prior-oxide layers regarding post-quench mechanical properties. Indeed the overall quantity of oxygen atoms diffusing into the sub-oxide metallic layers at high temperature is independent of the oxygen source: reduction of the prior-oxide or formation of a “fresh” oxide. At these oxidation temperatures, the impact of a prior-oxide

on the evolution of β_{Zr} ductile phase thickness is low, compared to the impact of a variation of the ductile-brittle oxygen concentration threshold as shown at 1200°C.

Two different tools have been used to simulate high temperature oxidation in Zr alloys: Ekinox numerical tool and DICTRA commercial software, both of them use the Zircobase thermodynamic database. Ekinox allows the simulation of oxygen diffusion profiles in α and β phases of Zr alloys during HT oxidation. It has also been successfully adapted in order to simulate the case of oxide dissolution in the substrate. Last, it was demonstrated that the model can be used to anticipate post-quenched mechanical properties of the material oxidized at high temperature knowing the post-quenched O concentration in β_{Zr} phase. Still, some improvements are needed in order to provide better descriptions of the phenomena: include the diffusion of other elements like Cr for EATF claddings and introduce a composition dependence of the diffusion coefficients. DICTRA gives account of such dependence of the diffusion coefficients, however, dimensional variations due to phase transformations are not taken into account. A common feature between both tools is the lack of reliable diffusion coefficients: experimental determinations of such data on model alloys are needed.

1.27.3.3 Ferrite δ Sigmatization in 316Nb steels³⁹

Stainless steels (as 316Nb) are used in the nuclear industry for components designed for high-temperature applications in hostile or corrosive environments, regarding their high corrosion resistance and mechanical properties at elevated temperatures. Many works⁴⁰⁻⁴² have demonstrated that after prolonged exposures to in-service conditions over a large range of temperatures, these alloys tend to embrittle. This is mainly due to the formation of secondary phases such as carbides ($M_{23}C_6$, M_6C and MC), nitrides (Cr_2N) and intermetallic phases (σ , χ , or Laves Phases). Among them, the σ phase can also have a detrimental effect on corrosion properties.⁴³⁻⁴⁹ In order to avoid intergranular corrosion in austenitic stainless steels, elements such as niobium are introduced, leading to “stabilized” austenitic stainless steels. Niobium addition improves both creep strength and corrosion resistance. Corrosion resistance is enhanced by the addition of Cr and Mo as well. Furthermore, these elements are known to promote σ -phase precipitation during long-term aging. The 316Nb stainless steels studied within this work contained (wt%): 19.30Cr, 12.50Ni, 2.70Mo, 1.40Mn, 0.40Si, 0.06C, less than 0.05N and Nb such $> 8 \times C$, but $< 1\%$. The alloys were preliminary annealed at 1100°C for 30 min. Thus, the microstructure is constituted by stable niobium carbonitrides embedded in a γ -austenitic matrix, elongated residual δ -ferrite islands are also observed. At last, σ -phase is also expected to precipitate inside γ -austenite grains. Yet, precipitation of σ -phase is also observed within ferrite islands during isothermal annealing or slow cooling from high temperature ($T > 1100^\circ C$) as shown in Fig. 7. We will show hereafter how thermodynamic and kinetic calculations allowed us to understand the phenomenon involved in this retransformation.

First, property diagrams were calculated using Thermo-Calc (TC) and MatCalc (MC) and the appropriate thermodynamic databases. They represent the variation of the mole fraction of phases at thermodynamic equilibrium as a function of temperature (Fig. 8). Both databases predict the precipitation of σ -phase inside γ -matrix.

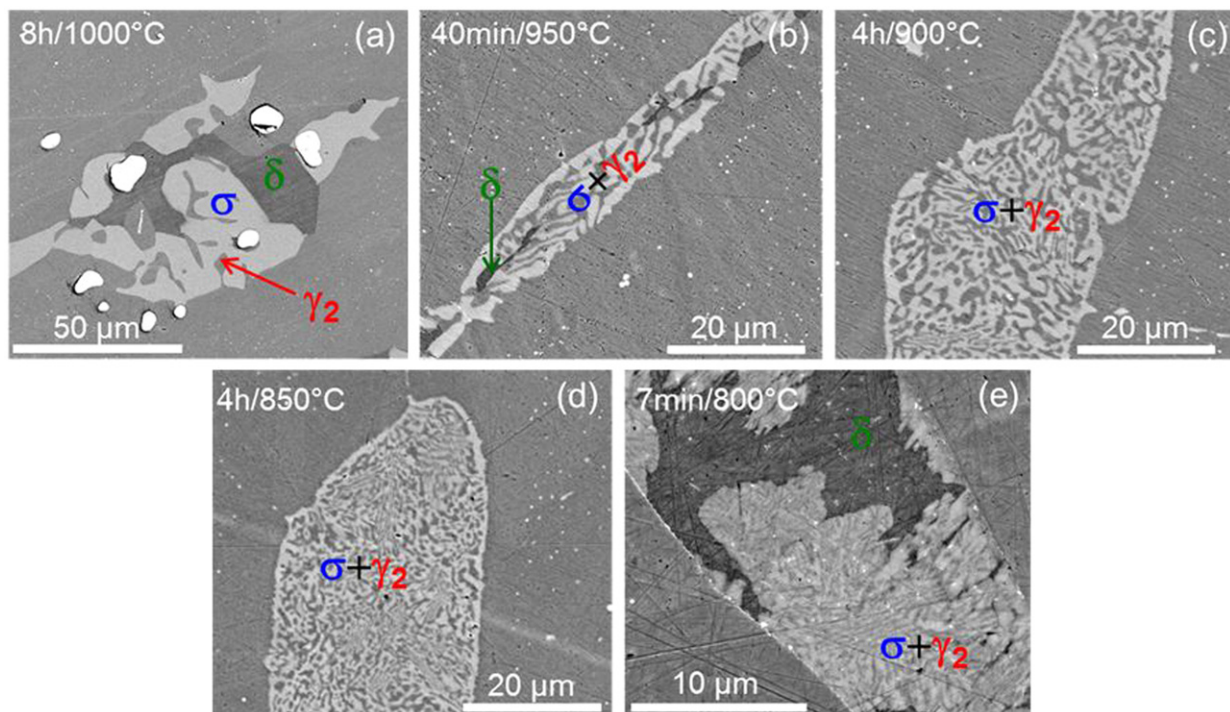


Fig. 7 SEM micrographs of residual δ ferrite after different isothermal annealings showing its progressive retransformation into a $\sigma + \gamma$ mixture. From Perron, A., Toffolon-Masclat, C., Ledoux, X., *et al.*, 2014. Understanding sigma-phase precipitation in a stabilized austenitic stainless steel (316Nb) through complementary CALPHAD-based and experimental investigations. *Acta Mater.* 79, 16–29.

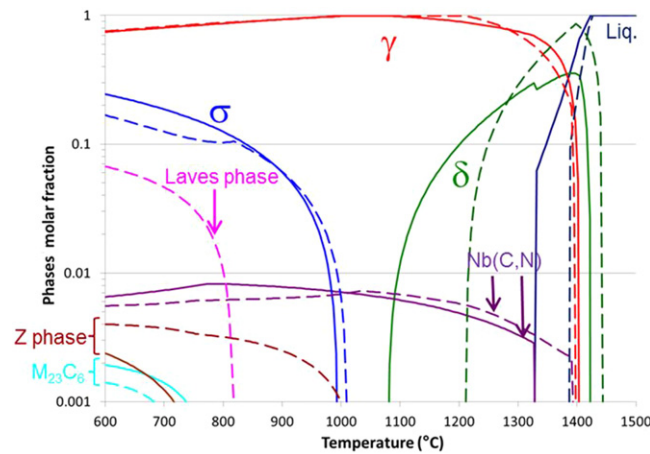


Fig. 8 Property diagram of 316Nb steel representing the mole fraction of phases at thermodynamic equilibrium as a function of temperature using TC and MC softwares (solid and dashed lines respectively). From Perron, A., Toffolon-Masclat, C., Ledoux, X., *et al.*, 2014. Understanding sigma-phase precipitation in a stabilized austenitic stainless steel (316Nb) through complementary CALPHAD-based and experimental investigations. *Acta Mater.* 79, 16–29.

In order to understand σ -phase precipitation in δ ferrite, the chemical composition of δ ferrite at the end of thermodynamic equilibrium has been considered to be the nominal composition. New property diagrams have thus been plotted (Fig. 9). Despite some discrepancy, TC and MC predict the precipitation of austenite and σ -phase according to the following eutectoid reaction: $\delta \rightarrow \sigma + \gamma$. These predictions are in very good agreement with the experimental observations made on different samples as illustrated in Fig. 7.

Finally, in order to fully grasp the sigmatization of δ ferrite, the quenching of δ ferrite embedded in a γ matrix has been simulated using DICTRA software. The following procedure was undertaken:

- (1) The chemical composition of the γ matrix was calculated at a temperature when $\sigma_{eq.}$ should start to precipitate according to TC (Fig. 7). This allowed a simplification of the system that is a removal of Nb, N and C thus preventing the precipitation of Nb(N,C);
- (2) Kinetic calculations involving more than four elements are numerically challenging using DICTRA, so the alloy composition was converted to an equivalent composition using a modified DeLong formula:

$$\text{Creq. (wt\%)} = [\text{Cr}] + 1.5[\text{Si}] + 0.5[\text{Nb}] \quad \text{Nieq. (wt\%)} = [\text{Ni}] + 30[\text{C}] + 30[\text{N}] + 0.5[\text{Mn}]$$

Knowing, from Badji,⁵⁰ that one of the factors controlling σ -phase growth is the diffusion of Mo, this element has been considered separately. The resulting equivalent chemical composition is: 20.13%Cr_{eq.}, 2.70% Mo and 13.97%Ni_{eq.}.

- (3) From this equivalent composition, an equilibrium calculation was made at a temperature corresponding to the end of solidification: 1300°C. The phase fractions obtained are comparable to those calculated for the system containing all the elements. Finally, the composition of the γ and δ phases were considered for kinetic calculations.
- (4) The system size for DICTRA calculations was defined from the different micrographs: 100 μm , corresponding to half-spacing between laths of residual ferrite was considered.

This simulation has been tested from 1300 to 600°C for cooling rates ranging from 2 to 100°C min⁻¹. An additional treatment has been considered: 60 h hold at 1150°C with 30°C min⁻¹ cooling rate. This treatment roughly represents 1150°C isothermal hold during thermomechanical processing.

σ -phase was not considered for these simulations giving informations on interface displacements and elements partitioning between metastable phases. The interface displacements as a function of temperature are presented in Fig. 10. Even for the slowest cooling rate, 2°C min⁻¹, the simulation do not predict a complete retransformation of δ ferrite into γ austenite.

The shrinkage of δ ferrite at the expense of γ austenite during cooling induces an increase in Cr and Mo contents and a decrease in Ni content in γ phase close to the interface. DICTRA simulations predict this phenomenon very well (Fig. 11). In order to relate it to the σ phase precipitation mechanism, the variation of Cr, Mo and Ni concentration profiles in δ ferrite has been plotted (Fig. 11(d)). It shows that close to the interface, Cr and Mo concentrations are high whereas Ni concentration is low. Equilibrium calculations made considering this concentration as a nominal one show that, in this particular case, σ precipitates directly from δ -ferrite. On the contrary, if one considers a nominal composition far from the interface, Cr and Mo contents decrease while Ni content increases. Thus, equilibrium calculations considering this new nominal composition tends to promote σ phase precipitation by an eutectoid transformation. It has been possible to determine the composition threshold

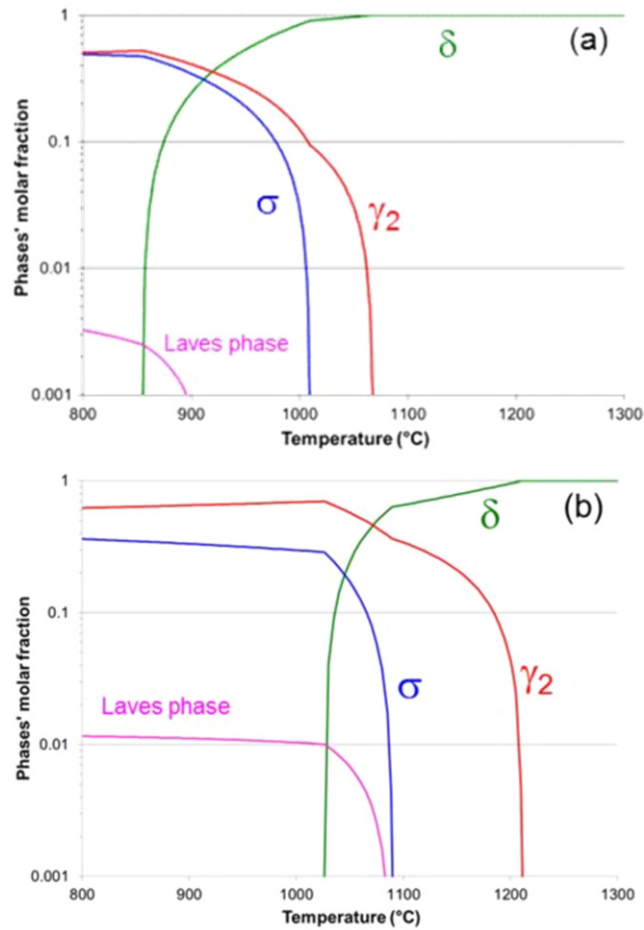


Fig. 9 Mole fraction of phases at thermodynamic equilibrium as a function of temperature considering the δ -ferrite composition at the end of thermodynamic equilibrium as the nominal composition, according to (a) TC and (b) MC. From Perron, A., Toffolon-Masclat, C., Ledoux, X., *et al.*, 2014. Understanding sigma-phase precipitation in a stabilized austenitic stainless steel (316Nb) through complementary CALPHAD-based and experimental investigations. *Acta Mater.* 79, 16–29.

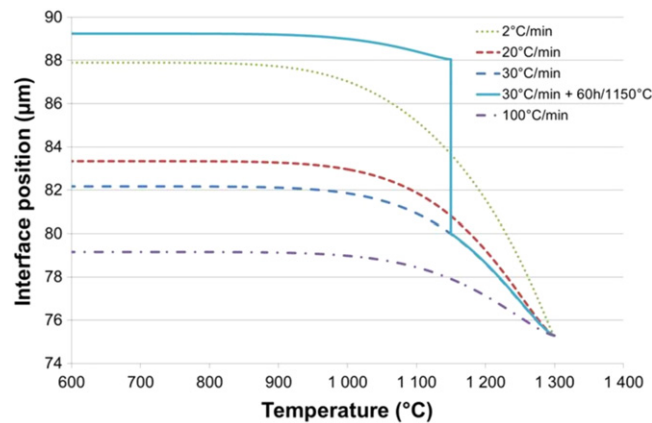


Fig. 10 Interface position between γ matrix and residual δ ferrite as a function of temperature for different cooling rates. From Perron, A., Toffolon-Masclat, C., Ledoux, X., *et al.*, 2014. Understanding sigma-phase precipitation in a stabilized austenitic stainless steel (316Nb) through complementary CALPHAD-based and experimental investigations. *Acta Mater.* 79, 16–29.

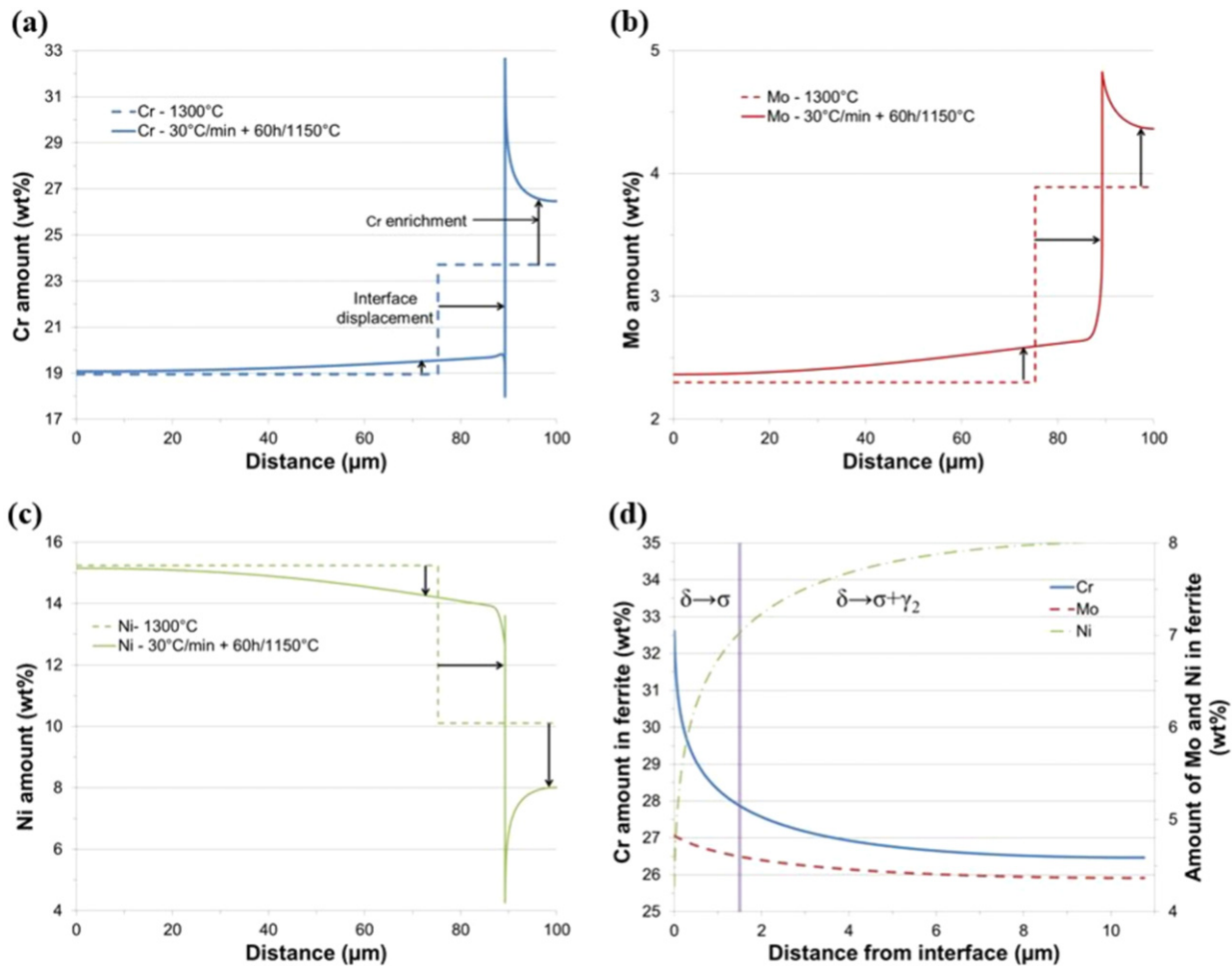


Fig. 11 Variation of Cr, Mo and Ni contents between an initial state of thermodynamic equilibrium (1300°C) and after thermal treatment (30°C min⁻¹ cooling rate with 60 h isothermal hold at 1500°C) using DICTRA. The dashed line corresponds to the initial system, while the solid line corresponds to the end of the thermal treatment (a)–(c). DICTRA-simulated Cr, Mo and Ni concentration profiles in δ ferrite after the thermal treatment, plotted as a function of the distance from γ/δ interface (d). The vertical line separates both types of σ-phase precipitation, depending on the chemical composition of ferrite. From Perron, A., Toffolon-Masclat, C., Ledoux, X., *et al.*, 2014. Understanding sigma-phase precipitation in a stabilized austenitic stainless steel (316Nb) through complementary CALPHAD-based and experimental investigations. *Acta Mater.* 79, 16–29.

between these two mechanisms: from the γ/δ interface up to a distance of 1.5 μm within δ ferrite, σ precipitates directly, beyond this distance, σ precipitates from eutectoid decomposition.

These statements have been verified experimentally by ElectronProbeMicroanalysis (EPMA). Indeed, the elements concentration profiles have been measured at the interface γ/δ for the reference state, that is, fast cooling rate (200°C min⁻¹) from high temperature, preventing the precipitation of σ phase.

The experimental measurements follow a similar trend: Cr and Mo increasing amounts at the interface and decreasing Ni amount (Fig. 12).

Finally, two experimental thermal treatments allowed the verification of the predicted mechanism of σ-phase precipitation: direct or eutectoid decomposition. These experiments show that after 5 min isothermal holding at 900°C, a σ-phase rim has precipitated at the interface δ/γ, this can be associated with the direct σ-phase precipitation (Fig. 13). When the isothermal treatment is extended, the eutectoid decomposition occurs within the δ ferrite island, meanwhile the σ-phase rim remains unchanged. This confirms that the direct precipitation of σ-phase from δ ferrite is mainly induced by the concentrations in this area.

Both thermodynamic and kinetic calculations have allowed a thorough study of σ-phase precipitation in 316Nb “stabilized” austenitic stainless steel. Thermodynamically, σ-phase is expected to precipitate at γ-austenite grain-boundaries via a common solid-state reaction.

However, owing to the presence of δ ferrite islands within the γ-austenite matrix, it has been shown, experimentally, that σ-phase is more susceptible to precipitate within this residual metastable phase.

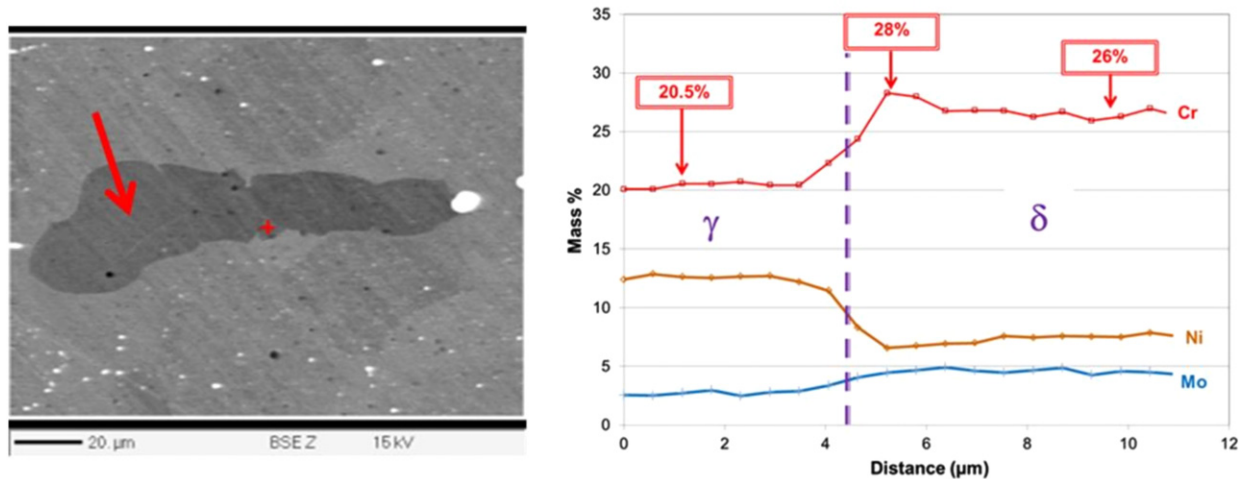


Fig. 12 SEM observation of a δ ferrite island in a reference state specimen: the red arrow represents EPMA measurements across the γ/δ interface (micrograph). The EPMA measurements are represented on the graph. From Perron, A., Toffolon-Masclat, C., Ledoux, X., *et al.*, 2014. Understanding sigma-phase precipitation in a stabilized austenitic stainless steel (316Nb) through complementary CALPHAD-based and experimental investigations. *Acta Mater.* 79, 16–29.

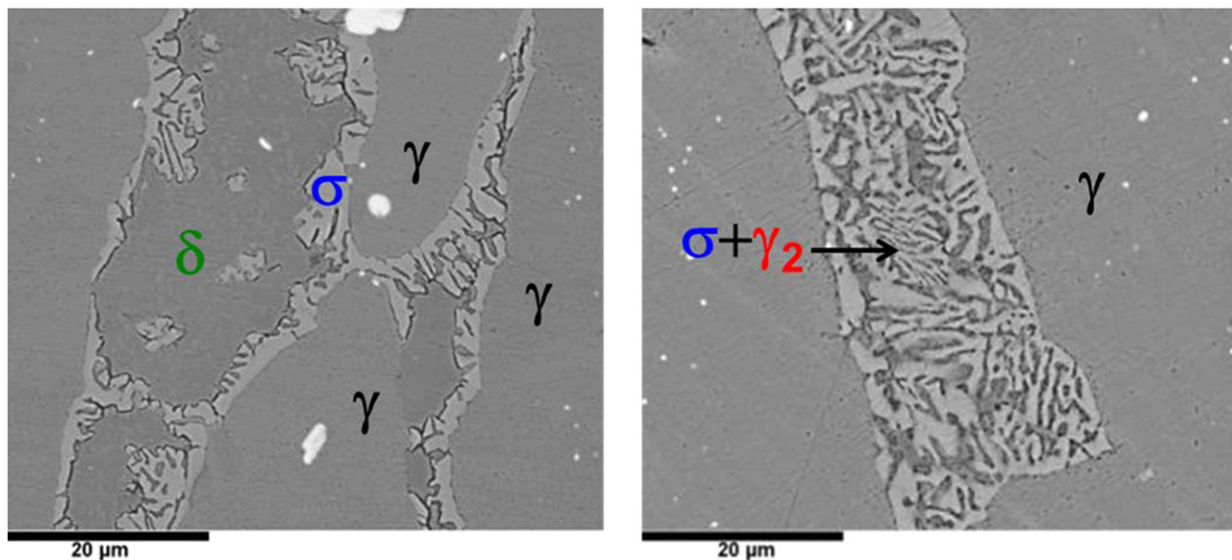


Fig. 13 SEM observation of a δ ferrite island after 5 min (left side) and 30 min (right side) isothermal hold at 900°C. From Perron, A., Toffolon-Masclat, C., Ledoux, X., *et al.*, 2014. Understanding sigma-phase precipitation in a stabilized austenitic stainless steel (316Nb) through complementary CALPHAD-based and experimental investigations. *Acta Mater.* 79, 16–29.

Thermokinetic calculations, using commercial softwares ThermoCalc, DICTRA and MatCalc, allowed understanding δ ferrite sigmatisation. Two different mechanisms related to the Cr, Mo and Ni concentration profiles have been suggested. The first one involves direct precipitation of σ -phase from δ ferrite, while the second one is controlled by the eutectoid decomposition of δ ferrite. Finally, it is shown that the precipitation kinetics of σ -phase in δ ferrite is much faster than equilibrium σ -phase precipitation within the γ matrix. However, it was not possible to simulate the real eutectoid transformation within the δ ferrite islands using DICTRA due to the closed nature of the software. Phase Field could be tested to simulate this reaction.

1.27.4 Precipitation

Precipitation is a particular type of transformation involving interfacial diffusion. Readers are referred to⁵¹ for an elaborate review of solid-state precipitation theories and associated calculation algorithms. In the next paragraphs, basic concepts of precipitation modeling using Classical Nucleation and Growth Theories (CNGTs) are presented.

Precipitation can be modeled at different scales. First of all, Density Functional Theory (DFT) (see Ref. 1) is used to calculate enthalpy of phases. Then, Molecular Dynamics (see Refs. 3,4) coupled to Kinetic Monte-Carlo (see Ref. 5) can be used to model the first stages of precipitation. Phase field is particularly adapted to study the morphogenesis of precipitates due to non-isotropic stress state (see Ref. 7). Then semi-predictive mean field models aim at simulating the precipitation behavior at longer time. Calphad-based commercial programs such as ThermoCalc (including Dictra and TC-Prisma) or Matcalc use combined thermodynamic database and diffusion database to model solid-state precipitation in multi-components systems. Finally, JMAK-type (Johnson-Mehl-Avrami-Kolmogorov) phenomenological models allow to kinetically describe the level of thermally activated phase transformation (recrystallization, precipitation) based on physical (activation energy) and no physical (arbitrary coefficients) parameters.

These different kinds of model involve complementary time and space scales. JMAK models are useful for modeling phase transformation in large components and occurring for hours and longer time but encounter difficulties to reproduce non-isothermal treatments and physical mechanisms.⁵² At the opposite, atomistic models are powerful tools to understand physical mechanisms but the time scale is reduced to approximately 10^{-6} s and involve very long time calculation for a limited number of atoms.^{53,54} For precipitation, a good compromise consists of thermokinetic model using CNGTs. This kind of model is described in the next section.

1.27.4.1 Classical Nucleation and Growth Theories

Classical Nucleation and Growth Theories (CNGTs) are widely used for the prediction of the evolution of a precipitate size distribution. CNGTs are based on the prediction of nucleation rate and growth rate of a population of precipitates. In the following, the nucleation and growth rate equation will be derived in the simple case of a spherical precipitate.

1.27.4.1.1 Nucleation

The nucleation rate dN/dt gives the flux of precipitates reaching the critical size r^* , above which they are stable and grow:

$$\frac{dN}{dt} = N_0 Z \beta^* \exp\left[-\frac{\Delta G^*}{k_B T}\right] I(t) \quad (18)$$

where N_0 is the nucleation site number density, Z is the Zeldovich factor, β^* is the condensation rate, ΔG^* is the energy barrier for nucleation, k_B is the Boltzmann constant, T is the temperature and $I(t)$ is an incubation coefficient varying from 0 to 1 with $I(0) = 0$ and $I(\infty) = 1$.

The energy barrier ΔG^* is given for spherical precipitates by:

$$\Delta G^* = \frac{16}{3} \pi \frac{\gamma^3}{(\Delta g_{ch} + \Delta g_{el})^2} \quad (19)$$

where γ is the precipitate/matrix interfacial energy, Δg_{el} is the elastic misfit energy and Δg_{ch} is the driving force for precipitation. For a precipitate containing N elements, the driving force is given by:

$$\Delta g_{ch} = \frac{1}{v_{at}^p} \sum_j^N \left[\mu_j(X_j) - \mu_j(X_j^i) \right] X_j^p \quad (20)$$

where X_j^p is the solute atom fraction of precipitates, v_{at}^p is the atomic volume of the precipitate and $\mu_j(X_j)$ is the chemical potential of element j in the solid solution of concentration X_j (X_j^i) is the solute concentration at equilibrium at matrix/precipitate interface. Chemical potentials can be estimated from thermodynamical databases or from solubility products of the literature.

The Zeldovich factor Z is calculated from the estimation of the stationary flux of n -mers reaching the critical size r^* assuming a Boltzmann distribution of unstable precipitates (detailed calculation in Ref. 55).

The condensation rate β^* has been approximated⁵⁵ and later generalized for multicomponent systems.^{56,57} Based on atomistic simulations, Clouet *et al.*^{53,54,58} proposed a form based on the solution of the diffusion equation:

$$\beta^* = \frac{4\pi r^*}{v_{at}^M} \left(\sum_j \frac{X_j^p}{D_j X_j} \right)^{-1} \quad (21)$$

where X_j is the solute content and D_j is the diffusion coefficient of element j .

The incubation coefficient $I(t)$ was originally proposed as $I(t) = \exp(-\tau/t)$ but later comparison with atomistic Monte-Carlo simulations led to the slightly different form: $I(t) = 1 - \exp[-t/\tau]$.⁵⁹ Note that this form is only valid for isothermal holding treatments.

1.27.4.1.2 Growth

The growth equation of spherical precipitates is obtained via Fick's diffusion equation assuming a stationary solute concentration profile of element j and equilibrium at matrix/precipitate interface:

$$\frac{dr}{dt} = \frac{D_j}{r} \frac{X_j^0 - X_j^i(r)}{\alpha X_j^p - X_j^i(r)} \quad (22)$$

where α is the ratio of atomic volumes of matrix and precipitates: $\alpha = v_{at}^M/v_{at}^P$ and X_j^0 is the alloy composition of element j . The equilibrium solute concentrations $X_j^i(r)$ are given by the Gibbs-Thomson equation (see Ref. 60,61):

$$\sum_j X_j^p \left[\mu_j(X_j^i(r)) - \mu_j(X_j^i(\infty)) \right] = \frac{2\gamma v_{at}^p}{r} \quad (23)$$

At each timestep, if the number of nuclei is larger than a critical value, a new class of precipitate is created with number density $N_i = dN/dt \times \Delta t$. Then all existing classes grow according to the solution of the non-linear system formed by Eqs. (22) and (23), leading to $r_i(t + \Delta t) = r_i(t) + dr/dt \times \Delta t$. Finally, the mass balance is performed to update the solute content of all solute species X_j via:

$$X_j = \frac{X_j^0 - \alpha X_j^p f^p}{1 - \alpha f^p} \quad (24)$$

where f^p is the volume fraction of precipitates:

$$f^p = \sum_i \frac{4}{3} \pi r_i^3 N_i \quad (25)$$

In order to get a smooth precipitate size distribution, it is sometimes necessary to add a new precipitate class between two existing ones or, eventually, to delete an existing class. Detail on class management can be found in Refs. 56,57.

The integration time step Δt is also optimized in such a way that it can increase exponentially (to correctly describe coarsening where precipitate mean radius varies as $\langle r \rangle \propto t^{1/3}$) and also decrease when time integration lead to unphysical results (*e.g.*, negative solute concentrations).

1.27.4.1.3 Implementations

Classical implementation of CNGTs are described by the so-called Numerical model of Kampman and Wagner (KWN).⁶² They have been more recently implemented in the form of a "multi-class" open softwares ("Multi-Preci" in Ref. 59 and "PreciSo" in Refs. 56,57). They are also proposed as accomplished commercial software systems ("Matcalc" in Refs. 63,64 and "TC-Prisma" in Ref. 65).

1.27.4.1.4 Limits of CNGTs

CNGTs are based on some important assumptions and contains limitations that hinder their application to simple systems:

- (1) In its basic formulation, interfacial energy is homogeneous and precipitates are spherical, which is far from reality in some systems (*e.g.*, β_{Nb}).

This limitation is partially solved in Matcalc software, where the interface energy is not fitted but rather calculated by counting the broken bonds between the particle and the Nearest Neighbors Broken Bonds (NNBB).⁶⁶ The interfacial energy is then linked to the enthalpy solution of the system by:

$$\gamma = \frac{n_S \cdot z_{S,eff}}{N \cdot z_{L,eff}} \cdot \Delta E_{sol} \quad (26)$$

with N , n_S , $z_{S,eff}$ et $z_{L,eff}$ respectively the number of nearest neighboring atoms, the number of atoms by surface area, the number of broken bonds per atom at the interface and the total number of bonds per atom.

- (2) Elastic misfit energy or external stress effects are poorly described and often not explicitly accounted for, leading to an unphysical concept of "effective" interfacial energy. This could be taken into account in relatively simple way. Indeed, the elastic energy takes action as soon as one coherent precipitate generates a distortion of the matrix lattice network close to the interface. This distortion is thus quantified by the degree of misfit between the interatomic distances of the lattice plans at the interface⁶⁷:

$$\delta = \frac{d_M - d_p}{d_p} \quad (27)$$

where d_M and d_p are the lattice parameter of the matrix and the precipitate, respectively. The elastic energy is then related to the degree of misfit by⁶⁷:

$$\Delta g_{el} = 3\mu\delta^2 r^3 \quad (28)$$

with μ the shear modulus and r the precipitate radius. This kind of improvement is implemented in Matcalc.

- (3) Calculation of nucleation rate is based on monomer (single solute atom) diffusion and Boltzmann statistics, conditions that are not valid for concentrated alloys
- (4) Diffusion fields around precipitates are supposed to be infinite (no impingement), which is not the case when volume fraction of precipitates is more than a few percents
- (5) Diffusion fields are supposed to be spherical, which does not hold for non-spherical precipitates or for precipitates growing in defects (*e.g.*, dislocations, grain boundaries)
- (6) The chemical composition of the precipitates is an input parameter. Metastable phases can compete with stable ones, but they have to be both defined thermodynamically a priori.

In the next section, we will present recent applications of GNGTs for nuclear applications.

1.27.4.2 Precipitation of Oxides in ODS Steels

Oxide-dispersion strengthened (ODS) steels owe their good high-temperature mechanical properties to a fine dispersion of nano-sized oxides that act as efficient obstacles for dislocations and grain boundaries. Depending upon the chemical composition of the initial powders and the processing route parameters, various kinds of oxides can precipitate. They have been the subject of numerous characterization studies at the nanoscale, including transmission electron microscopy (TEM), neutron or X-Rays small-angle scattering (SANS or SAXS) and more recently atom-probe tomography (APT). The finest dispersoids found so far in ODS steels appear to be either Y_2O_3 or more recently $Y_2Ti_2O_7$, where titanium gives rise to an increased number density of finer particles.⁶⁸ The very first published work on this system was that of Guisca in 1939, who prepared the mixed oxide $Y_2Ti_2O_7$ and showed that the phase had a face-centered pyrochlore-type structure.⁶⁹ They suggested that a continuous solid solution range between $Y_2Ti_2O_7$ and Y_2O_3 might exist. Other complex oxides such as orthorhombic Y_2TiO_5 were entirely described by Mumme *et al.*⁷⁰ In two high-chromium steels containing aluminum (4.5 wt%) with and without titanium, Hsiung *et al.* observed solely complex Ti-free $Y_4Al_2O_9$, and a few $YAlO_3$. A complete list of forming oxides in steels can be found in Ref. 71.

These nanoparticles exhibit an extraordinary thermal stability, even at temperatures close to the solidus of the ferritic matrix. Very recently, nanoscale to atomic scale studies were used to bring some insight into this coarsening resistance. One theory highlights the role of a large amount of oxygen vacancies ($\approx 10\%$) that stabilize the clusters.⁷² Another by Ribis and de Carlan demonstrated that the morphology of the particles $Y_2Ti_2O_7$ evolve upon heating in order to minimize their energy within the system.⁷³ The shape transition from spherical to cubical geometry was described as a way to reduce the elastic distortion created at the interfaces.

Based on these observations, the benefits of having a precipitation model are quite straightforward: the nanoscale characterization can be tedious and expensive whereas the prediction assisted by modeling of the precipitation state as a function of the thermo-mechanical treatments could be a precious help to estimate the mechanical properties.

CNGTs modeling consists in calculating the driving force of the formation of a possible compound (phase) from a supersaturated solid solution. In ODS steels, various studies based on TEM, SANS, XRD, APT, lead to contradictory conclusions on whether yttrium, oxygen atoms transform into a solid solution in the iron matrix. Clustering of yttrium and titanium-rich particles was observed by APT after a certain milling time,^{74–76} as a proof of imperfect solid solution, even if these subnanometric clusters are quite homogeneously distributed in the powders. Also, after annealing or consolidation at high temperature, the clusters tend to crystallize and form stoichiometric phases.^{72,73,77,78} Thus, the starting point before high-temperature consolidation still deals with the need of diffusion-governed atoms transport to form well-defined, crystalline precipitates.

1.27.4.2.1 Modeling homogeneous precipitation of oxides in ODS steels with PreciSo

The first attempt to model precipitation with classic nucleation, growth and coarsening theories (CNGTs) was performed on the Y_2O_3 compound by Hin *et al.*⁷⁹ Both interface energy and diffusion coefficient of yttrium in α -iron were fitted with SANS data. Boulnat *et al.*⁸⁰ proposed to go further by studying the precipitation kinetics of both Y_2O_3 and complex $Y_2Ti_2O_7$ nanoparticles in ODS steels with and without titanium and processed by hot isostatic pressing or rapid spark plasma sintering (Table 1).

PreciSo^{83–85} was used to apply the NGCTs on ODS precipitation modeling. As such, it was assumed that:

- (1) The precipitation was homogeneous. There was no preferential nucleation on defects such as dislocations or grain boundaries.
- (2) The diffusion process that governs the precipitate growth was ruled by the diffusivity of the slowest element, that is yttrium. This was applied to the model only if the condition $\{\forall \text{ element } i, D_Y^i/D_i^z < 10^{-4}\}$ was verified.

All the thermodynamic and thermokinetic parameters are given in Table 2.

The solubility product was derived from first principle calculations of the enthalpy formation of oxides in steels performed by Chinnappan.⁷¹

Table 1 Composition in solute elements, heat treatments and resulting precipitate states of ODS steels used for precipitation modeling

	Cr	Y	O	Ti	Treatment	R_m [nm]	N_p [m^{-3}]	Ref.
(wt%)	18	0.24	0.06	0	850°C – 1 h	1.5	9.1×10^{23}	68
(at%)	19.2	0.15	0.22	0	1100°C – 1 h	6	9.0×10^{21}	
(wt%)	13.9	0.21	0.05	0	HIP 850°C – 3 h	1.43	1.1×10^{24}	81
(at%)	15	0.13	0.18	0	HIP 1100°C – 3 h	5.39	7.9×10^{21}	
(wt%)	13.9	0.21	0.05	0.4	HIP 850°C – 3 h	1.25	2.57×10^{24}	
(at%)	15	0.13	0.18	0.4	HIP 1000°C – 3 h	1.53	8.5×10^{23}	81
					HIP 1100°C – 3 h	1.71	3.02×10^{23}	
(wt%)	13.9	0.16	0.15	0.32	SPS 1100°C – 20 min	1.5	$3. \times 10^{24}$	82

Table 2 Thermodynamic and diffusion parameters from literature and used for the precipitation model of Y_2O_3 and $Y_2Ti_2O_7$

	Parameter	Value	Source
α -ferrite	Lattice parameter	$a = 2.886 \times 10^{-10} \text{ m}$	XRD 86
	Atomic volume	$v_{at}^{\alpha} = 1.202 \times 10^{-29} \text{ m}^3$	86
	Diffusion coefficient	$D^0 [\text{m}^2 \text{ s}^{-1}] \text{ Q} [\text{J mol}^{-1}]$	
	Yttrium	$D_Y^0 = 1 \times 10^{-5} \text{ 299,102}$	87
	Titanium	$D_{Ti}^{\alpha} = 0.21 \text{ 293,200}$	88
	Oxygen	$D_O^{\alpha} = 4 \times 10^{-5} \text{ 166,942}$	89
		$D_O^{\alpha} = 2.9 \times 10^{-7} \text{ 89,500}$	90
		$D_O^{\alpha} = 4 \times 10^{-5} \text{ 161,129}$	87
BCC Y_2O_3		$D_O^{\alpha} = 3 \times 10^{-5} \text{ 139,193}$	80
	Atomic volume	$v_{at}^{Y_2O_3} = 1.49 \times 10^{-29} \text{ m}^3$	80
	Solubility product	$\log(K_S) = -20000/T - 4$	
	Interfacial energy	$\gamma^{Y_2O_3} = 0.35 \text{ J m}^{-2}$	TEM 73
Pyrochlore type $Y_2Ti_2O_7$		$\gamma^{Y_2O_3} = 0.4 \text{ J m}^{-2}$	87
		$\gamma^{Y_2O_3} = 0.60 \text{ J m}^{-2}$	80
	Atomic volume	$v_{at}^{Y_2Ti_2O_7} = 9.9 \times 10^{-30} \text{ m}^3$	80
	Solubility product	$\log(K_S) = -19000/T - 25$	
	Interfacial energy	$\gamma^{Y_2Ti_2O_7} = 0.25 \text{ J m}^{-2}$	TEM 73
		$\gamma^{Y_2Ti_2O_7} = 0.48 \text{ J m}^{-2}$	80

The interfacial energy, fitted with SANS data as 0.4 J m^{-2} , was consistent with semi-coherent particles. A close value was found by Ribis *et al.* (0.35 J m^{-2}).⁷³ Please note that Barnard *et al.*⁹¹ determined the interfacial energy by *ab initio* calculations and found 3.06 J m^{-2} , which is far much higher.

The diffusion of yttrium not only governs the nucleation onset but also determines the growth rate since it is the slowest solute element in the precipitate compared to titanium and oxygen. The 'calculated' diffusion coefficient of yttrium in α -iron suggested that yttrium diffused 400 times lower than iron self-diffusion at 850°C ,⁷⁹ which confirmed the role of yttrium as diffusion-limitant species for the precipitation process.

However, there is no reliable direct experimental measurement of yttrium coefficient diffusion in either ferrite or austenite, which makes the coefficient after⁷⁹ a unique value to work with.⁷³ An alternative expression was determined by Murali *et al.*⁹² by density functional theory (DFT). The diffusion coefficient determined by Hin was fitted with experimental data in a limited temperature range, up to 1150°C . This was indeed restricted to the range of typical consolidation temperatures of ODS steels. However, all recent studies prove that the coarsening behavior of Y_2O_3 and more importantly $Y_2Ti_2O_7$ is observed at higher temperature, typically 1200°C , 1300°C and 1400°C . Consequently, if the diffusion coefficient accurately reproduces the precipitation kinetics of Y_2O_3 during consolidation, it seems to overestimate the diffusivity of yttrium at higher temperature. This induces a much too high coarsening rate compared to that calculated from the aforementioned studies at very high temperatures.

As a consequence, a new expression of the diffusion coefficient was proposed⁸⁰:

$$D_Y = 10^{-7} \text{ m}^2/\text{s} \exp\left(\frac{-260 \text{ kJ/mol}}{R_g T}\right) \quad (29)$$

1.27.4.2.1.1 Precipitation of Y_2O_3

Since $Y_2Ti_2O_7$ are known to preferentially form in titanium, yttrium containing steels, only Ti-free ODS steels were considered to model the precipitation behavior of Y_2O_3 . The ODS steels with published experimental nanoscale characterization that were used for this study are summarized in Table 1. In order to compare to the precipitation state of ODS steels produced by HIPing or extrusion, non-isothermal treatments were simulated at the possible consolidation temperatures (850 , 1000 , 1100°C).

Fig. 14 describes the temporal evolution of the simulated mean radius and number density of Y_2O_3 and the comparison of published experimental data of the same composition from Ratti *et al.*⁹³ The simulation also reproduces consistent results at 850°C but slightly underestimates the mean radius observed by SANS at 1100°C . Since at 1000°C and 1100°C the mean radius of Y_2O_3 after Alinger and Hin is at the contrary overestimated, one can conclude that there is no biased tendency of the model to underestimate/overestimate the coarsening behavior of Y_2O_3 . Instead, the numerical results are in very good agreement with the experimental data from SANS. The interfacial energy giving rise to the best match between experiments and simulations is $\gamma_{Y_2O_3} = 0.6 \text{ J m}^{-2}$, which is higher than those from either Hin (0.4 J m^{-2}) or Ribis (0.35 J m^{-2}) but this is still consistent with semi-coherent particles.

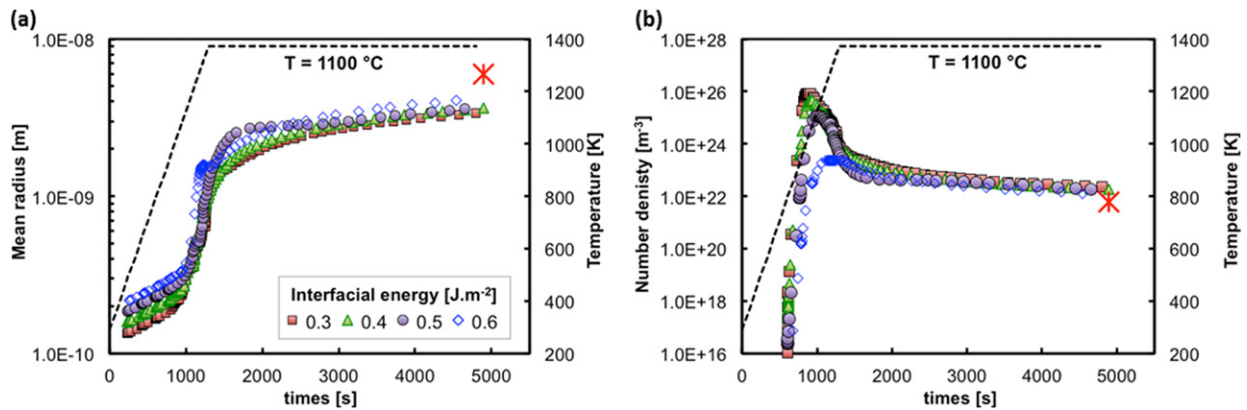


Fig. 14 Time evolution (linear scale) of simulated Mean radius and number density of Y_2O_3 particles during non-isothermal pressure-free heat treatments at $1100^\circ C$. SANS data are from Ratti, M., Leuvrey, D., Mathon, M.H., de Carlan, Y., 2009. Influence of titanium on nano-cluster (Y, Ti, O) stability in ODS ferritic materials. *J. Nucl. Mater.* 386–388, 540–543. Ratti, M., 2010. Development of new ferritic/martensitic steels for RNR-Na tube cladding materials, translated from ‘Développement de nouvelles nuances d’aciers ferritiques/martensitiques pour le gainage d’éléments combustibles des Réacteurs à Neutrons Rapides au sodium’ PhD Thesis. Institut Polytechnique de Grenoble.

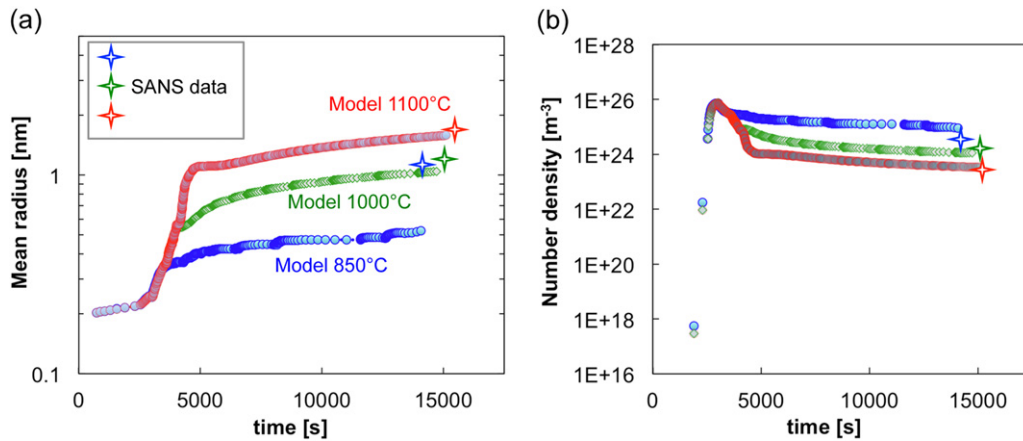


Fig. 15 Time evolution (linear scale) of simulated Mean Radius and Number Density of $Y_2Ti_2O_7$ particles during non-isothermal heat treatments at (a)–(b) $850^\circ C$, $1000^\circ C$ and $1100^\circ C$. SANS data are from Alinger, M.J., 2004. On the Formation and Stability of Nanometer Scale Precipitates in Ferritic Alloys During Processing and High Temperature Service. PhD Thesis. Santa Barbara: University of California. Alinger, M.J., Odette, G.R., Hoelzer, D.T., 2009. On the role of alloy composition and processing parameters in nanocluster formation and dispersion strengthening in nanostructured ferritic alloys. *Acta Mater.* 57 (2), 392–406.

1.27.4.2.1.2 Precipitation of $Y_2Ti_2O_7$

The simulated precipitation behavior of $Y_2Ti_2O_7$ during HIPing is represented in Fig. 15. The kinetics is quite similar to that of Y_2O_3 since it is governed by the diffusion of yttrium. The main difference is the higher number density for $Y_2Ti_2O_7$ compared to Y_2O_3 , which can be explained by the larger solute content available for the precipitation of $Y_2Ti_2O_7$.

The present model was also applied to the precipitation kinetics during SPS consolidation, showing a good comparison between experimental data collected by SANS, ATP and TEM and numerical data from the model,⁸⁰ despite an exaggerated coarsening kinetics for the model. Indeed, the coarsening behavior is handled by the Gibbs-Thomson effect through Eq. (23). This effect was applied assuming a spherical shape of the precipitates, which may not be fully accurate. Indeed, Ribis showed that a deviation from spherical into ellipsoidal or cuboidal shape was observed upon annealing at high temperature. In this context, the coarsening kinetics would be impacted, which may explain the difference in coarsening kinetics between experimental and numerical results.

1.27.4.2.1.3 Conclusion on PreciSo modeling

The model predicts the thermal stability of Y_2O_3 and $Y_2Ti_2O_7$ but seems to overestimate the coarsening stage compared to the published experimental data. The number density from the simulation is higher than that measured on SPSed ODS steels. This can be explained by the assumption of a unique and stoichiometric phase in the simulation whereas in the reality the particles may observe variation in the composition, not only in yttrium, titanium and oxygen but also in the enrichment in other solutes like

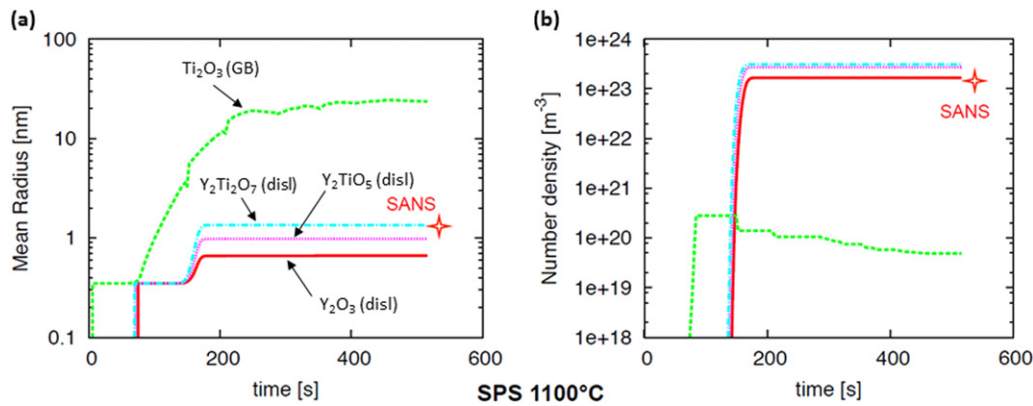


Fig. 16 Evolution of simulated mean radius and number density of $Y_2Ti_2O_7$, Y_2TiO_5 , Y_2O_3 and Ti_2O_3 particles during SPS at $1100^\circ C$.

aluminum, silicon or chromium. The latter has been located in nanosized particles⁹⁴ or under the form of a shell surrounding the particles.⁹⁵ Most importantly, the effect of morphological change upon heating was not taken into account in the present model.

1.27.4.2.2 Modeling heterogeneous and multi-components precipitation in ODS steels with MatCalc

MatCalc was also assessed to model the precipitation of oxides in ODS steels, under the license 5.44 and the thermodynamic database *McFe2*.

Besides, heterogeneous nucleation was taken into account for the simulations using Matcalc. Since these materials are strongly deformed during mechanical alloying, a high density of dislocations and subgrain boundaries are observed, as highlighted by Salles *et al.*⁹⁶ using synchrotron X-Ray diffraction during *in situ* annealing. Thus, binary Y_2O_3 and complex Y-Ti-O populations were assumed to nucleate on dislocations. Besides, binary titanium oxides were assumed to form at grain boundaries. Indeed, the latter most likely form at the interfaces between consolidated powder particles, as illustrated by a FIB-3D characterization in Ref. 82. The nucleation at grain boundaries with a grain size of $50 \mu m$ was chosen, which corresponds to the mean diameter of the milled powder particles. In this particular configuration, grain boundary diffusion was applied.

Non-isothermal treatments simulating SPS or HIP treatments were used for precipitation simulations. MatCalc, like PreciSo for homogeneous precipitation, predicts the nucleation of nanoparticles within the first minutes of the consolidation cycles, typically during the heating stage (Fig. 16).

Complex Ti_2O_3 and $Y_2Ti_2O_7$ possess an equivalent number density, around $2 \times 10^{23} m^{-3}$, whereas binary Y_2O_3 has a number density two times lower. Considering that dislocations act as nucleation sites, the nucleation site density N_{disl} can be calculated using the following equation [Ref. 51 Chapter 2.4]:

$$N_{disl} = \frac{\rho}{a} \quad (30)$$

with ρ the dislocation density and a the lattice parameter. For $\rho = 10^{15} m^{-2}$ and $a = 0.29 nm$, $N_{disl} = 3.5 \times 10^{24} m^{-3}$. The three populations of oxides Y_2O_3 , $Y_2Ti_2O_7$ and Y_2TiO_5 fill a cumulated density of around $10^{24} m^{-3}$, which is of the same order of magnitude that the dislocation nucleation site density.

Also, the mean radius is constant after the nucleation is completed, which can correspond to a regime where growth and dissolution occur simultaneously. This stage is particularly long compared to what is simulated by PreciSo. The completion of very long annealing treatment actually gives rise to coarsening (not shown here).

Precipitation models based on CNGTs can reproduce various precipitation kinetics of oxides in ferritic steels. However, further improvements are needed. Homogeneous nucleation from a solid solution was assumed in the PreciSo calculations, which is debatable. Clusters of Y-O can constitute nucleation sites for Y-Ti-O particles, as well as dislocations present after mechanical alloying. Taking into account the competition between several types of oxides (Y_2O_3 , $Y_2Ti_2O_7$, etc) would also be necessary to understand the relative stability of these compounds upon the treatments, for different ODS steels. Commercial softwares like Matcalc are much more achieved in their present form (connection with databases, interfacial energy calculation, misfit elastic energy), but the modifications of the CNGTs equations are easier in more simple and open software. However, note that authors of Matcalc welcome collaborations on new developments of their models and software.

1.27.4.3 Precipitation of Cu in Fe

Embrittlement of Nuclear Reactor Pressure Vessels (RPV) can occur during ageing due to the presence of Cu nanoprecipitates. Despite the relative complexity of the precipitation sequence (body-centered cubic (bcc) \rightarrow 9R \rightarrow face-centered cubic (fcc)), the binary iron-copper system is quite often used as a model alloy to validate precipitation models, due to the spherical nature of precipitates and the fact that copper precipitates are reported to be pure copper even in the earlier stages of formation.

Classical Nucleation and Growth Theories have been used on a binary Fe-1.4wt%Cu binary alloy to treat nucleation, growth and coarsening as concomitant processes (as in Ref. 62,97). In this section, we will use the PreciSo software to predict the precipitation kinetics of copper in iron.

To account for the loss of coherency of precipitates, a size-dependent interfacial energy is introduced. As the bcc to fcc transition is usually observed for particles larger than $r_t = 3$ nm,^{62,98} the following form for γ has been chosen (see more details in Ref. 56)

$$\gamma = \min \left[\gamma_{\text{bcc}} + \frac{r}{r_t} (\gamma_{\text{fcc}} - \gamma_{\text{bcc}}); \gamma_{\text{fcc}} \right] \quad (31)$$

All parameters used in this simulation are recalled in Table 3.

Fig. 17 shows the time evolution of precipitate mean radius and number density. The mean radius approach is compared with SANS^{20,34} and SAXS experiments³² performed on binary Fe-Cu alloys at 500 and 600°C. The agreement is quite good in the coarsening regime in view of the simplicity of this approach: homogeneous nucleation, mean field approach, no impingement of precipitate diffusion fields (all precipitates lying within a solid solution, which solute fraction is updated at each time step). However, it can be observed that the precipitation kinetics during the growth stage is too fast compared to experiments with such a simple model.

Based on atomistic simulations,¹⁰⁰ Jourdan *et al.*¹⁰¹ accounted for abnormal Cu cluster mobility to improve CNGTs in a cluster dynamics model. More recently Stechauner and Kozeschnik¹⁰² also accounted for this abnormal cluster mobility and also interfacial free energy effects and successfully compared experimental and modeled TTP diagram in the temperature range 450–700°C as shown in Fig. 18.

Precipitation of Cu in iron is a good example of a system for which CNGTs cannot simply describe all features of the precipitation kinetics (volume fraction, radii, number density). Atomistic modeling highlighted the important effect of cluster mobility in the diffusion of Cu. From this findings, experimental results could be much better described within the mean field approach by modifying the basis of CNGTs, namely the diffusion of Cu in Fe in nucleation and growth equations.

Table 3 Parameters used to model copper precipitation in iron with PreciSo

Parameter	Value	Ref.
X^p	1	
X^0	0.0125	
$\log_{10}(X^i)$	$\frac{5.77 \times 10^6 \text{K}^2}{T^2} - \frac{1.58 \times 10^4 \text{K}}{T} + 7.89$	98
D	$6 \times 10^8 \text{ m}^2/\text{s} \exp\left(\frac{166.4 \text{ kJ/mol}}{RT}\right)$	99
γ_{bcc}	0.3 J/m ²	62
γ_{fcc}	0.6 J/m ²	62
$V_{at}^{P,M}$	$1.5 \times 10^{-29} \text{ m}^3$	

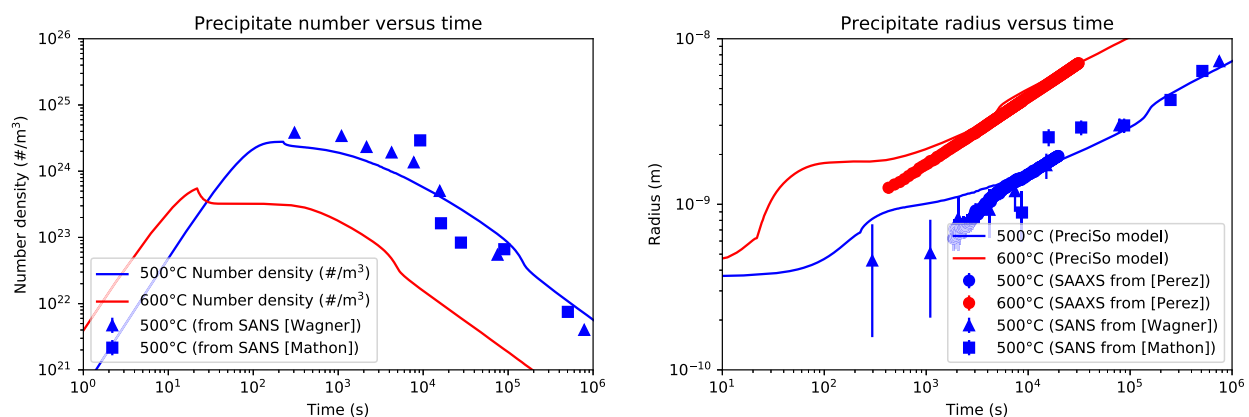


Fig. 17 Kinetic evolution of the precipitate number density (left), radius (center) and volume fraction (right) as predicted by the PreciSo model. Solid points refer to experimental data from nuclear and magnetic SANS experiments on Fe-1.38 at% Cu. From Wagner, R., Kampmann, R., Voorhees, P.W., 2006. Homogeneous second-phase precipitation. Materials Science and Technology. Wiley-VCH Verlag GmbH & Co. KGaA. Mathon, M.H., Barbu, A., Dunstetter, F., *et al.*, 1997. Experimental study and modeling of copper precipitation under electron irradiation in dilute FeCu binary alloys. J. Nucl. Mater. 245, 224–237, and SAXS experiments on Fe-1.25 at% Cu, Perez, M., Perrard, F., Massardier, V., *et al.*, 2005. Low temperature solubility of copper in iron: Experimental study using thermoelectric power, small angle X-ray scattering and tomographic atom probe. Philos. Mag. 85 (20), 2197–2210.

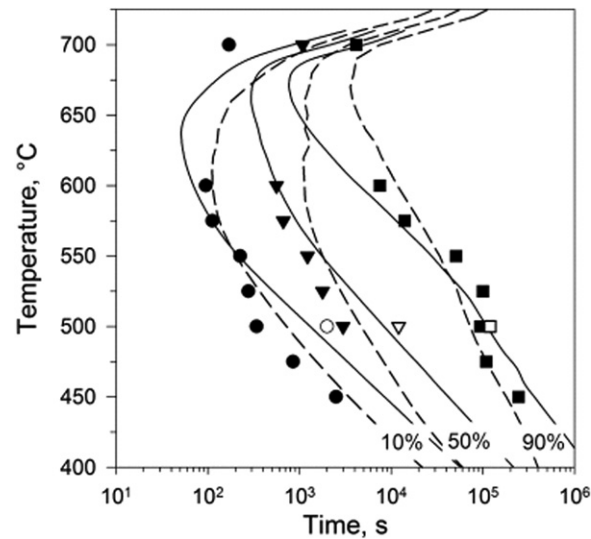


Fig. 18 Isothermal TTP diagram calculated with Matcalc and compared with experimental data of Perez *et al.* and Goodman *et al.* shown in filled and empty symbols, respectively. Solid and dashed lines show different parametrization. Reproduced from Perez, M., Perrard, F., Massardier, V., *et al.*, 2005. Low temperature solubility of copper in iron: Experimental study using thermoelectric power, small angle X-ray scattering and tomographic atom probe. *Philos. Mag.* 85 (20), 2197–2210. Goodman, S.R., Brenner, S.S., Low, J.R., 1973. An FIM-atom probe study of the precipitation of copper from Iron-1.4 at. pct copper. Part i: Field-ion microscopy. *Metall. Trans.* 4 (10), 2363–2369. Stechauner, G., Kozeschnik, E., 2015. Thermo-kinetic modeling of Cu precipitation in α -Fe. *Acta Mater.* 100, 135–146.

1.27.4.4 Precipitation of Carbides in Bainitic Steels¹⁰³

2.25Cr-1Mo steel is being considered potential candidate as pressure vessel material for future light water reactors considering its good mechanical properties in quenched and tempered conditions¹⁰⁴ and its good resistance to radiation-induced embrittlement compared to usual pressure vessel steel.¹⁰⁵

Depending on the thermal treatments applied to this material, various types of carbides can be found, namely, M_3C , M_2C , M_7C_3 , $M_{23}C_6$ and M_6C .¹⁰⁶ Their size, nature and fraction can have a direct influence on mechanical properties. Thus, a good knowledge of carbide precipitation through manufacturing heat treatments is of high interest. The carbides precipitation sequences have been determined experimentally on this material by Dépinoy *et al.*¹⁰³ The overall precipitation sequence has been identified as the result of three precipitation sub-sequences occurring simultaneously. Cementite (M_3C) particles first precipitate from the decomposition of retained austenite. M_7C_3 carbides start to nucleate at the interface between cementite and matrix and grow by diffusion of Cr and C atoms from the parent M_3C phase. In a second time, molybdenum carbides, M_2C , precipitate homogeneously from the matrix. Then, $M_{23}C_6$ particles precipitate, mainly at interfaces, but also at dislocations within the bainitic laths. Finally, these three sub-sequences interact with each other with increasing time and temperature: the growth of $M_{23}C_6$ induces the dissolution of neighboring less stable M_2C and M_7C_3 carbides.

In order to test the assumptions made on the carbides precipitation sub-sequences, thermokinetic calculations were performed in order to reproduce the experimental observations. For this purpose, the system was represented as follows.

1.27.4.4.1 Model assumptions

1.27.4.4.1.1 Matrix

Bainite can be represented in this framework as elongated ferritic subgrains (laths) which share similar crystallographic orientations within the grain (packet), where a carbon partitioning occurs between the (perfect) crystal lattice and the dislocations. First simulations were conducted with such a representation of the matrix. However, the results proved to be highly sensitive to the lath size, which value has not been determined precisely. Thus, the matrix was simulated at a larger scale, where so-called grains are prior austenite grains and so-called subgrains are the bainitic packets. The assumption lying behind this representation of bainite is that the total dislocation density in the material is partly due to the low-angle lath boundaries in a given packet. Thus, no difference is made between carbide precipitation at intralath dislocations and at lath boundaries. Moreover, the presence of retained austenite at interfaces cannot be directly taken into account. Instead, calculations were carried out with carbon trapped at subgrain boundaries, *i.e.*, at bainitic packet boundaries. For comparison purposes, calculations were also performed with carbon trapped at dislocations. In such case, the relative evolution of carbide phase fraction was the same, but the kinetics was not satisfactorily represented.

The dislocation density in the matrix, ρ , was determined according to the empirical Eq. (32) given by Zajac *et al.*¹⁰⁷ where B_S is the bainite start transformation temperature in the case of isothermal transformation, in Kelvin. As a first assumption, this temperature will be taken as the one in the case of continuous cooling. For the considered cooling rate of 0.3°C/s, $B_S = 793.15K$,

$\rho = 1 \times 10^{15} \text{ m}^{-2}$. This order of magnitude seems reasonable when considering a bainitic microstructure.

$$\log_{10}(\rho) = 9.28480 + \frac{6880.73\text{K}}{B_S} - \frac{1780360\text{K}^2}{B_S^2} \quad (32)$$

1.27.4.4.1.2 Carbides

Carbides to be considered in calculations were selected according to reported experimental observations, *i.e.*, M_3C , M_7C_3 , $M_{23}C_6$ and M_2C . The nucleation stages were represented in the model by considering the experimental work from¹⁰³: cementite transforms from ε -carbides, M_7C_3 nucleates at the interface between cementite and the matrix, and $M_{23}C_6$ and M_2C nucleate on their own. From experimental results, cementite was assumed to nucleate from the retained austenite around 500–600°C. However, such transformation cannot be taken into account in these calculations. Thus, in order to simulate nucleation of cementite at these temperatures, ε -carbides were artificially added to the system, and set up to transform into cementite upon heating at the experimentally observed temperature.

The chemical composition of the nucleus is a key parameter for modeling precipitation of carbides. Cementite and M_7C_3 carbides are not concerned by this parameter since they result from the transformation of pre-existing carbide; no control on their nucleus composition can be made. M_2C and $M_{23}C_6$ nuclei composition were calculated under an ortho-equilibrium assumption. The model calculates the chemical composition by assuming that the precipitates nucleate with their equilibrium composition. For $M_{23}C_6$ carbides, such assumption is in good agreement with experimental measurements. For M_2C carbides, this assumption is more representative of the experimental results than a para-equilibrium composition, which assumes that the nucleus composition is the same as the one of the matrix, except for carbon.

Nucleation sites were chosen according to the results from experimental observations: M_2C carbides were assumed to precipitate homogeneously within the laths, $M_{23}C_6$ carbides were assumed to precipitate at dislocations since these latter partly correspond to actual lath boundaries, and cementite and M_7C_3 carbides (and therefore ε -carbides in these calculations) were assumed to precipitate both at dislocations and at subgrain boundaries (SGB).

A shape factor was applied to M_3C , M_2C and $M_{23}C_6$ precipitates due to their particular geometry, respectively branch-like, needle-like and rod-like. The shape factor for branch-like and rod-like was set to 5; the one for needle-like was set to 10.

1.27.4.4.1.3 Nucleation and growth parameters

It should be pointed out that the abovementioned hypotheses alone, coupled with the default parameters in MatCalc, result in calculated phase fraction and size within the right order of magnitude. However, the precipitation/dissolution of carbides is not well described. For instance, $M_{23}C_6$ carbides grow very slowly at 650°C, while no more M_7C_3 are present after only 1 h at 725°C. Moreover, the balance between nucleation and growth for $M_{23}C_6$ do not describe accurately the experimental results. Thus, several parameters were adjusted in order to change the temperature at which carbides start to precipitate and their nucleation rate. The chosen values for these parameters are only guessed ones, since no information is available from literature, to the author's knowledge. However, these slight changes result in better agreement with experimental data.

- (1) The critical radius of carbides is the minimum size of a carbide embryo that is stable and begins to grow (*i.e.*, minimum nucleus size). Decreasing the value of this parameter results in a higher nucleation rate, and nucleation occurs at lower temperature. This parameter was set to 0.5 nm for all carbides with the exception of M_7C_3 for which it was set at 0.55 nm in order to increase the transformation temperature for the $M_3C \rightarrow M_7C_3$ reaction. Note that these values may even be lower than the size of the crystal unit cell (that contains a lot of atoms, though, for some carbides).
- (2) Nucleation rates can be decreased by decreasing the nucleation constant, resulting in a lower number fraction of carbides. The default value of this parameter is 1; its value was decreased down to 0.5 for M_7C_3 carbides in order to reduce the rate of transformation from cementite, and down to 0.4 for $M_{23}C_6$ carbides in order to avoid a too massive precipitation upon heating.

Summary of all nucleation conditions and values of model parameters for all types of carbides is made in [Table 4](#).

Heat treatments numerically applied in the simulations were chosen in accordance with the experimental ones, namely, a heating step at $0.333^\circ\text{C s}^{-1}$ (2°C min^{-1}), then an isothermal holding for times up to 30 h, followed by a quench at 100°C s^{-1} in order to simulate the water quench. No evolution of carbides occurs during this quench, thus they will not be discussed. Temperatures for the isothermal step range from 650°C to 725°C.

1.27.4.4.2 Comparison with experimental results and discussions

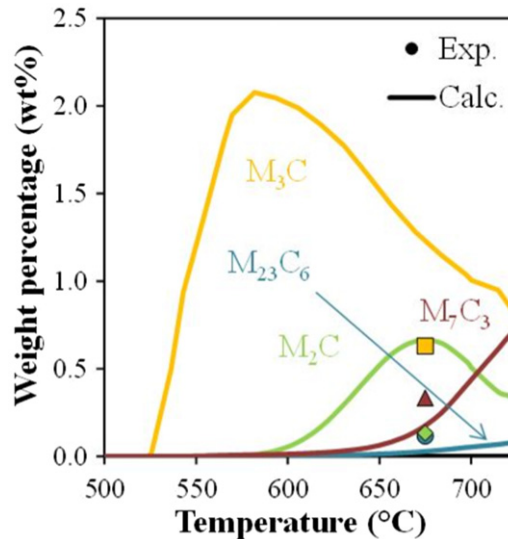
1.27.4.4.2.1 Evolution of carbide phase fractions

The evolution of carbide phase fraction with temperature during heating up to 725°C is shown in [Fig. 19](#). Since ε -carbides are only taken into account in order to simulate the precipitation of cementite at 520°C, they are not represented in this figure. From results given by the model, 80% of cementite is located at dislocations, which is in good agreement with experimental results, since in this model dislocations also account for lath boundaries.

Slight differences are found between experimental measurements and calculations, especially regarding the precipitation of M_2C carbides which is too strong, however at higher temperature their phase fraction decrease down to 0.3 wt% due to the precipitation of M_7C_3 carbides. Despite these slight differences, rather good agreement is found.

Table 4 Summary of nucleation mechanisms and carbide model parameters

	M_3C	M_7C_3	M_2C	$M_{23}C_6$
Nucleation sites	Same as ϵ -carbides	M_3C surface	Matrix	Dislocations
Nucleus composition	Direct transformation from ϵ -carbides	M_3C	Ortho-equilibrium	Ortho-equilibrium
Critical radius (nm)	0.5	0.55	0.5	0.4
Nucleation constant	1 (default)	0.5	1 (default)	0.3
Shape factor	5 (rod)	1 (sphere)	10 (needle)	5 (rod)

**Fig. 19** Evolution of carbide phase fraction upon heating.

The evolution of phase fraction with time during the isothermal step at 650°C, 675°C, 700°C and 725°C is shown in Fig. 20. General good agreement is found with the experimental results. However, in the calculations M_7C_3 precipitate too rapidly, leading to a too fast dissolution of cementite and a too high phase fraction of M_7C_3 . At 700°C and 725°C, growth of $M_{23}C_6$ is slowed down due to the elevated stability of M_7C_3 carbides. Moreover, at these temperatures, M_2C carbides are dissolving rapidly due to the too low dissolution temperature predicted for these carbides, while it happens experimentally for longer times. Such change in the thermodynamic equilibrium conditions might explain the differences between model predictions and experimental measurements. Slight differences at other temperatures are also observed: M_7C_3 carbides appear to be too stable, while M_2C carbides precipitate too massively at low times, as already stated. However, the general trend is respected.

1.27.4.4.2.2 Size evolution of carbides

The evolution of the characteristic dimensions of carbides with holding time at several temperatures is shown in Fig. 21. The characteristic dimension is the mean diameter for M_7C_3 carbides and the mean length for elongated M_2C , $M_{23}C_6$ and M_3C carbides. Experimental measurements were made from TEM observations, for an average number of 15 measurements per carbide per tempering condition. These dimensions are likely to obey a log-normal distribution, explaining the high standard-deviations for $M_{23}C_6$. It should be pointed out that the calculated number density of carbides remains stable between their nucleation upon heating and their final dissolution. Thus, growth is the only phenomenon that occurs during isothermal holding and that accounts for the change in phase fraction.

Very good agreement is found for M_7C_3 and M_2C carbides. The general trend for $M_{23}C_6$ carbides is fairly well represented; however one should notice that their growth appears to be too rapid. This is due to a bad balance between nucleation and growth of these carbides using the chosen parameters: in the calculations, less carbides are precipitating but they are growing faster when compared to experimental observations.

1.27.4.4.2.3 Elements concentration variation in solid solution

A comparison between the normalized amounts of both chromium and molybdenum in solid solution and in the carbides at 675°C is shown in Fig. 22. A good agreement is shown, except for the molybdenum content after 3 h, once again due to the too extensive precipitation of M_2C carbides predicted during the first hours of tempering by the model.

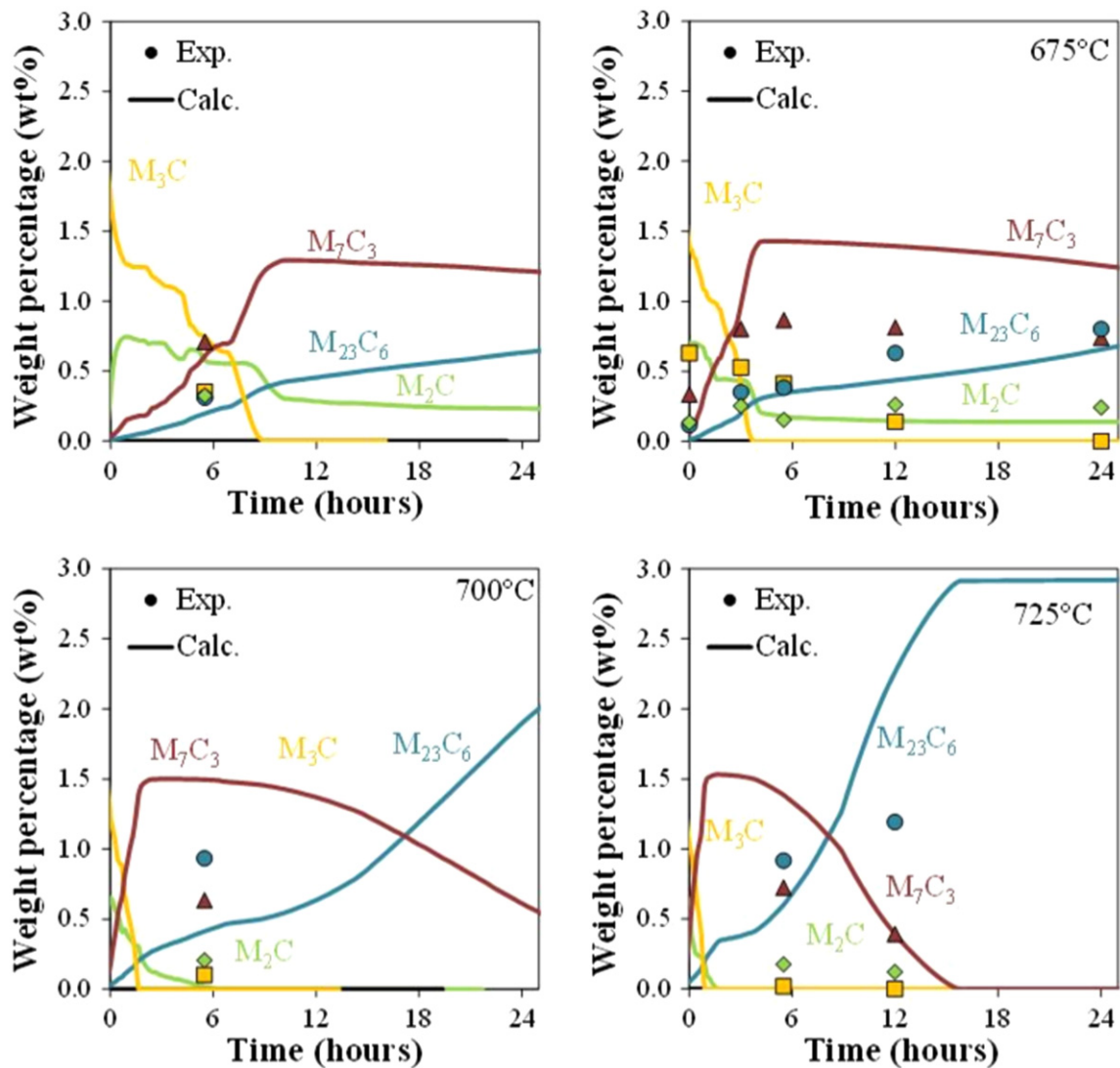


Fig. 20 Evolution of carbide phase fraction upon isothermal holding at different temperatures.

Experimental observations are rather successfully reproduced using the following nucleation conditions: nucleation of M_7C_3 carbides at the surface of cementite and separate nucleation of $M_{23}C_6$ and M_2C carbides inside the matrix. The growth of $M_{23}C_6$ and dissolution of M_7C_3 carbides are interrelated due to chromium diffusion. Still, there exists some limitations of the model: the more significant one concerns the relative amounts of metallic elements in cementite and M_7C_3 carbides. In both cases, Cr content is over estimated. Regarding cementite, this can be attributed to the nucleation mechanism considered: direct transformation from ε -carbides, while experimentally, they result from retained austenite decomposition. In the case of M_7C_3 carbides, it is more likely that the calculation of the nucleus composition does not represent the reality.

1.27.4.5 Precipitation of β_{Nb} in Zr Alloys

In Zr-Nb alloys used as nuclear fuel cladding tubes in nuclear reactors, it is mandatory to anticipate the behavior of β_{Zr} metastable phases in the final product. In the case of M5TM alloys, optimal properties, that is improved corrosion properties, are obtained for microstructures containing fine and homogeneously distributed equilibrium β_{Nb} phases within α_{Zr} matrix.¹⁰⁸ β_{Zr} metastable phases can remain, for instance, after fabrication process, depending on the thermal treatments applied or after welding operations. Thus, knowing the time necessary to precipitate equilibrium phases in Zr-Nb alloys at temperatures below 600°C (α_{Zr} temperature range) is of high industrial interest.

In order to properly study the precipitation kinetics of β_{Nb} phase, two opposite initial microstructures have been studied: the first one containing Nb in (supersaturated) solid solution and the second one containing β_{Zr} metastable phases (enriched in Nb). Zirconium alloys with different amounts of Nb have been studied. The first microstructure was achieved by thermally treating the alloy in the β phase domain at 1045°C and then water quenching it. This thermal treatment leads to a lath "Widmanstätten" type microstructure as shown in Fig. 23(a). In order to obtain the second microstructure, a similar heat treatment was applied, followed

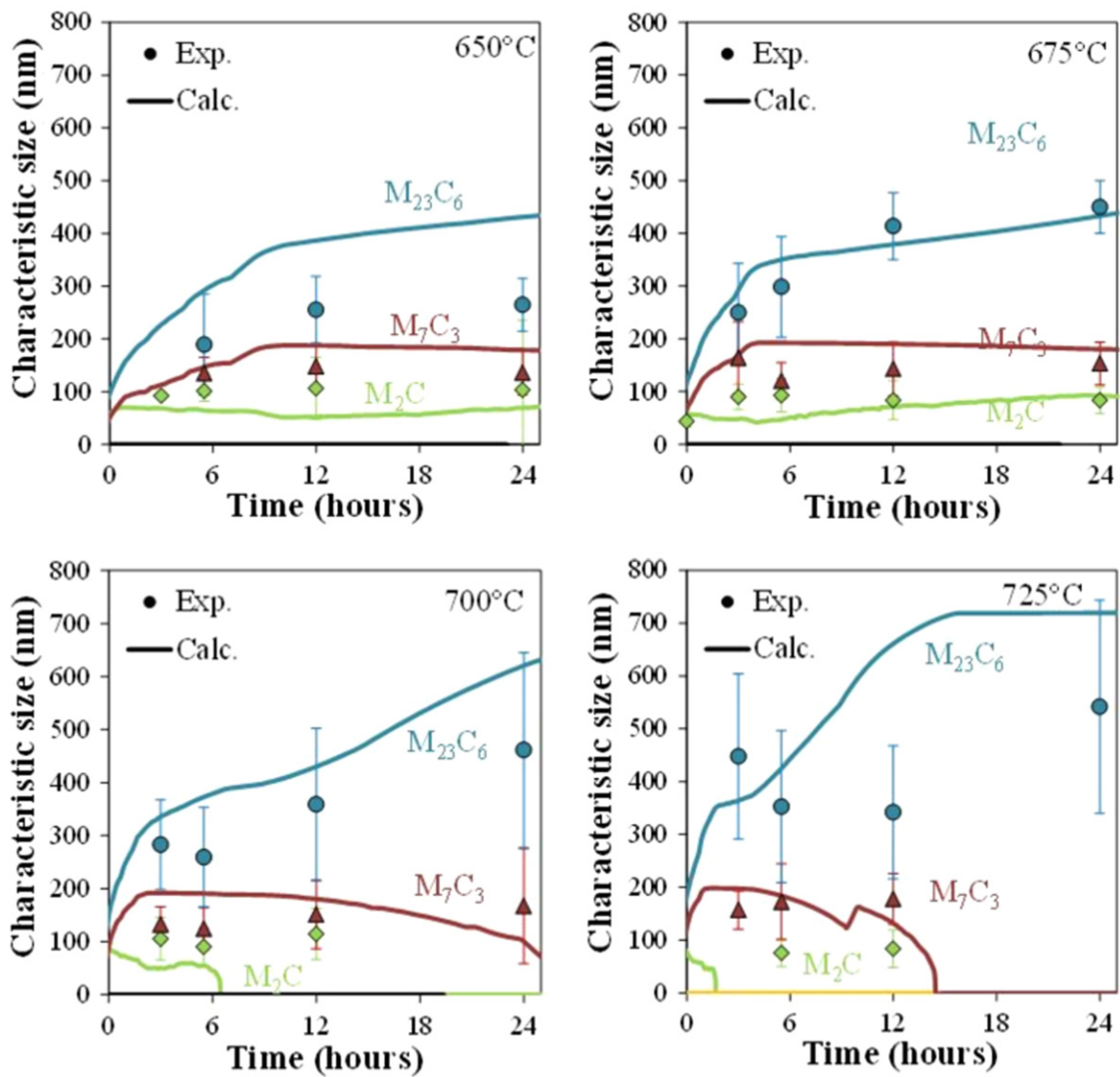


Fig. 21 Evolution of carbide characteristic dimension during the isothermal holding step.

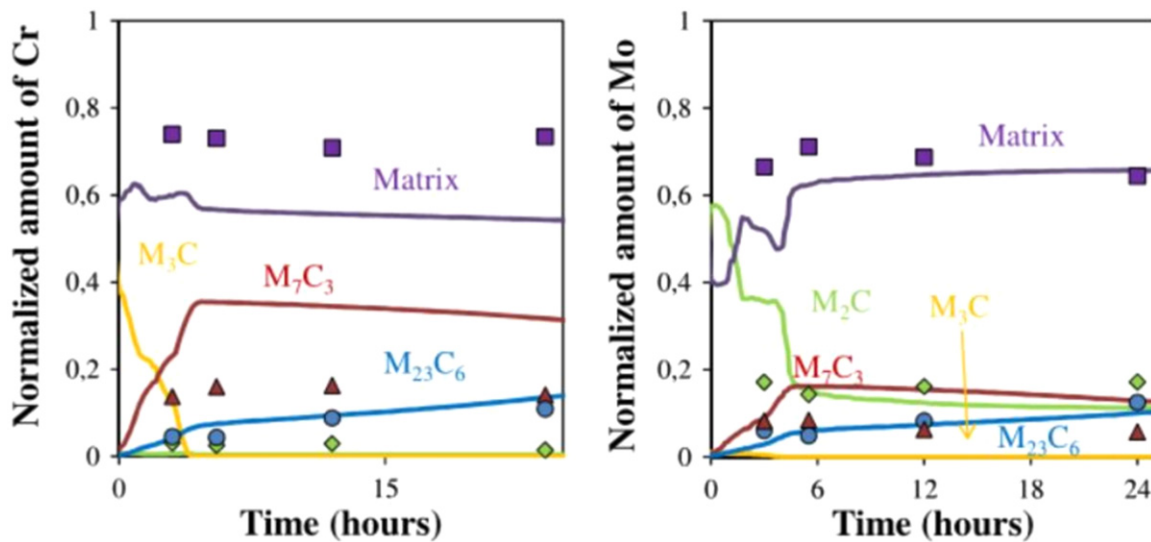


Fig. 22 Evolution with time of the normalized amount of carbide forming elements in solid solution and carbides at 675°C for: chromium (left) and molybdenum (right).

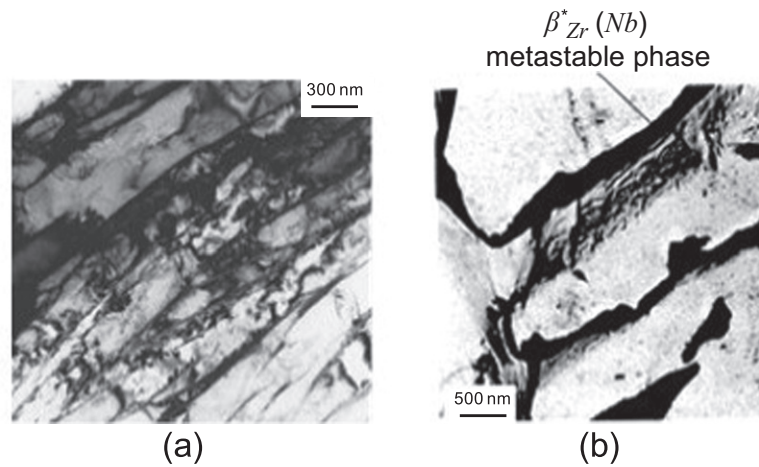


Fig. 23 TEM micrographs of a Zr-2.5%Nb heat treated at 1045°C and (a) water quenched, (b) slow cooled (1°C/min).

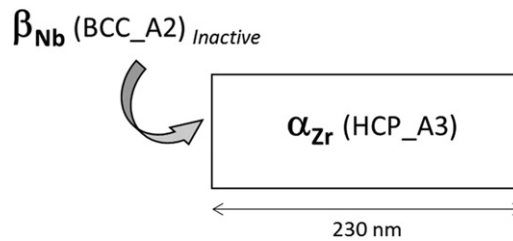


Fig. 24 Scheme of the initial calculation cell considered for the Zr-2.5%Nb β quenched.

by a slow cooling rate (1°C/min). In this microstructure, the retained metastable Nb enriched β_{Zr} phase is located at the interfaces between lamellae (Fig. 23(b)). The β_{Nb} precipitation kinetic has been followed experimentally by Differential Scanning Calorimetry (DSC). It was shown that, after thermal annealing at 570°C, applying a subsequent DSC cycle up to the $\alpha + \beta$ or β temperature range allows an indirect quantification of this precipitation kinetics by measuring the enthalpy associated with the on-heating $\alpha_{Zr} + \beta_{Nb} \rightarrow \alpha_{Zr} + \beta_{Zr}$ transformation. The results can be found in Ref. 109. For the simulations, the size of the cells has been taken equal to half the width of the lamellae, taking into account that β_{Nb} particles precipitate are located at the α -lamellae interfaces. In the case of quenched microstructure, at the beginning of the simulation, only one phase is active: α_{Zr} (HCP_A3) supersaturated in Nb. β_{Nb} (BCC_A2) phase is located at one side of the cell and is considered as inactive (Fig. 24).

This has been tested for two different Nb contents: 2.5 and 0.65 wt%. In both cases, β_{Nb} precipitation occurs quite rapidly, as shown in Fig. 25, the calculated precipitation kinetic shows good agreement with the experimental measurements derived from DSC.

For the slow cooled microstructure, two regions are considered at the beginning of the simulation. The first one contains the matrix α_{Zr} (HCP_A3) and the second one the metastable β_{Zr} phases enriched in Nb (20 wt%), see Fig. 26. Zr alloys containing different amounts of Nb, *i.e.*, 1 and 2.5 wt%, have been tested and compared to experimental results. During the calculation, metastable β_{Zr} phases (BCC_A2) dissolve quite rapidly and then the precipitation of β_{Nb} phases occurs for annealing times which are in good agreements with the experimental ones (Fig. 27).

Good results are obtained in this example using DICTRA software. Still, some limitations, like the choice of an average lath-size and the absence of nucleation rate, could be overtaken using tools like Matcalc or Preciso.

1.27.5 Outlooks

In this article, computational kinetics has been applied to different complex cases of transformations involving interface diffusion or precipitation in steels and zirconium alloys. Different tools have been tested depending on the phenomena to be studied: commercial softwares like ThermoCalc, Dictra and MatCalc or home-made ones like Preciso or Ekinox-Zr. In each case, the modelization is overall satisfactory, however some scientific issues still need to be overcome:

- (1) The lack of reliable (i) thermodynamics data, particularly for metastable phases, and, (ii) diffusion coefficients hinders accuracy of predictions;
- (2) Accurate experimental measurements (*i.e.*, precipitate volume fraction) are sometimes hard to find

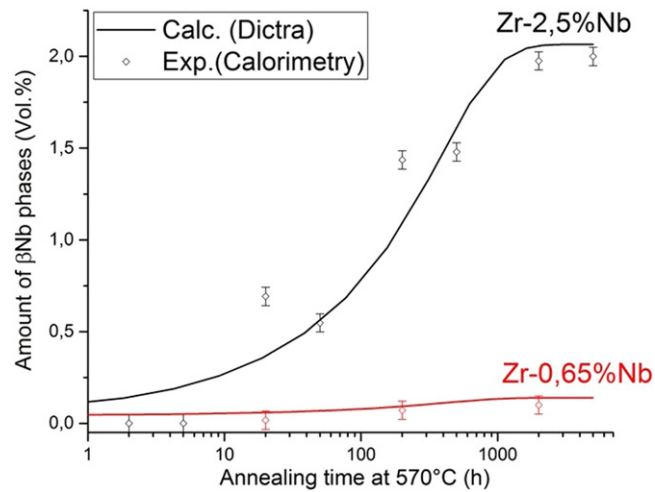


Fig. 25 Variation of the volume percentage of β_{Nb} phases from an as-quenched microstructure as a function of the annealing time at 570°C: comparison between DICTRA calculations and experimental measurements for Zr alloys containing 0.65 and 2.5 wt% Nb.

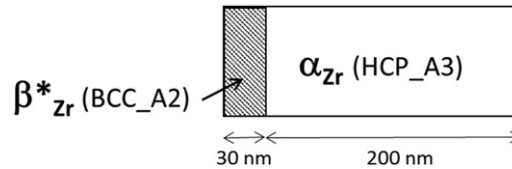


Fig. 26 Scheme of the initial cell considered for the Zr-2.5% Nb slow cooled.

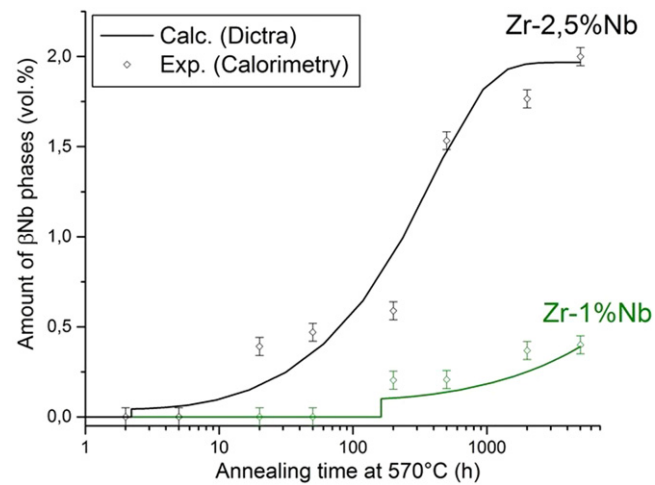


Fig. 27 Variation of the volume percentage of β_{Nb} phases from a slow cooled microstructure as a function of the annealing time at 570°C: comparison between DICTRA calculations and experimental measurements for Zr alloys containing 1 and 2.5 wt% Nb.

- (3) Connection with simulations at smaller scale (DFT, atomic, *etc.*) are far from obvious;
- (4) The closed nature of commercial software may restrict their development.

Therefore, there might exist expectations for the development of intermediate tools between commercial software and homemade tools. Such tools may benefit from active communities like the informal international collaboration around OpenCalphad.

Finally, the reader is encouraged to contact any author of this article to deploy and use Preciso or Ekinox-Zr softwares, and/or to participate to high quality MatCalc and ThermoCalc/Dictra training sessions.

Acknowledgments

The authors would like to acknowledge Arnaud Allera and Thibaut Chaise for their contribution on the PreciSo software and its python shell.

See also: 1.04 Radiation-Induced Effects on Microstructure. 1.14 Toward the Use of Ion Irradiation to Predict Reactor Irradiation Effects. 1.16 Ab Initio Electronic Structure Calculations for Nuclear Materials. 1.17 Interatomic Potential Development. 1.18 Molecular Dynamics. 1.20 Primary Radiation Damage Formation in Solids. 1.21 Atomic-Level Dislocation Dynamics in Irradiated Metals. 1.23 Reaction Rate Theory. 1.26 Computational Thermodynamics: Application to Nuclear Materials. 2.07 Fission Product Chemistry in Oxide Fuels

References

- Crocobette, J.P., Willaime, F., 2012. Ab initio electronic structure calculations for nuclear materials. In: Konings, R.J.M. (Ed.), *Comprehensive Nuclear Materials*, vol. 2. Elsevier.
- Malerba, L., 2012. Large scale integrated programs. In: Konings, R.J.M. (Ed.), *Comprehensive Nuclear Materials*, vol. 2. Elsevier.
- Cai, W., Li, J., Yip, S., 2012. Molecular dynamics. In: Konings, R.J.M. (Ed.), *Comprehensive Nuclear Materials*, vol. 2. Elsevier.
- Ackland, G., 2012. Interatomic potential development. In: Konings, R.J.M. (Ed.), *Comprehensive Nuclear Materials*, vol. 2. Elsevier.
- Becquart, C.S., Wirth, B.D., 2012. Kinetic Monte Carlo simulations of irradiation effects. In: Konings, R.J.M. (Ed.), *Comprehensive Nuclear Materials*, vol. 2. Elsevier.
- Ghoniem, N.M., 2012. Dislocation dynamics simulations of defects in irradiated materials. In: Konings, R.J.M. (Ed.), *Comprehensive Nuclear Materials*, vol. 2. Elsevier.
- Bellon, P., 2012. Phase field methods. In: Konings, R.J.M. (Ed.), *Comprehensive Nuclear Materials*, vol. 2. Elsevier.
- Purdy, G.R., Bréchet, Y.J.M., 2001. Transformations involving interfacial diffusion. In: Kostorz, G. (Ed.), *Phase Transformations in Materials*. Wiley-VCH Verlag GmbH.
- Besmann, T.M., 2012. Computational thermodynamics: Application to nuclear materials. In: Konings, R.J.M. (Ed.), *Comprehensive Nuclear Materials*, vol. 1. Elsevier.
- Gueneau, C., 2012. Computational thermodynamics: Application to nuclear materials. In: Konings, R.J.M. (Ed.), *Comprehensive Nuclear Materials*, vol. 2. Elsevier.
- Gouné, M., Danoix, F., Ågren, J., *et al.*, 2015. Overview of the current issues in austenite to ferrite transformation and the role of migrating interfaces therein for low alloyed steels. *Mater. Sci. Eng. R: Rep.* 92, 1–38.
- Wycliffe, P.A., Purdy, G.R., Embury, J.D., 1981. Growth of austenite in the intercritical annealing of Fe-C-Mn dual phase steels. *Can. Metall. Q.: Can. J. Metall. Mater. Sci.* 20 (3), 339–350.
- Atkinson, C., Akbay, T., Reed, R.C., 1995. Theory for reaustenitisation from ferrite/cementite mixtures in Fe-C-X steels. *Acta Metall. Mater.* 43 (5), 2013–2031.
- Lai, Q., Gouné, M., Perlade, A., *et al.*, 2016. Mechanism of austenite formation from spheroidized microstructure in an intermediate Fe-0.1C-3.5Mn steel. *Metall. Mater. Trans. A* 47 (7), 3375–3386.
- Ollat, M., Militzer, M., Massardier, V., *et al.*, 2018. Mixed-mode model for ferrite-to-austenite phase transformation in dual-phase steel. *Comput. Mater. Sci.* 149, 282–290.
- Chantrenne, P., Massardier, V., Perez, M., *et al.*, 2019. Diffusion model for austenite formation kinetics during inter-critical annealing of dual-phase steels. *Modell. Simul. Mater. Sci. Eng.* 27 (6).
- Kattner, U.R., 1997. The thermodynamic model of multicomponent phase equilibria. *JOM* 49 (12), 14–19.
- Andersson, J.-O., Helander, T., Höglund, L., Shi, P., Sundman, B., 2002. Thermo-calc & DICTRA, computational tools for materials science. *Calphad* 26 (2), 273–312.
- Larsson, H., 2014. A model for 1D multiphase moving phase boundary simulations under local equilibrium conditions. *Calphad* 47, 1–8.
- Krielaart, G.P., Sietsma, J., van der Zwaag, S., 1997. Ferrite formation in Fe-C alloys during austenite decomposition under non-equilibrium interface conditions. *Mater. Sci. Eng. A* 237 (2), 216–223.
- Sietsma, J., van der Zwaag, S., 2004. A concise model for mixed-mode phase transformations in the solid state. *Acta Mater.* 52 (14), 4143–4152.
- Bos, C., Sietsma, J., 2007. A mixed-mode model for partitioning phase transformations. *Scr. Mater.* 57 (12), 1085–1088.
- Bos, C., Sietsma, J., 2009. Application of the maximum driving force concept for solid-state partitioning phase transformations in multi-component systems. *Acta Mater.* 57 (1), 136–144.
- Zurob, H.S., Panahi, D., Hutchinson, C.R., Brechet, Y., 2013. Self-consistent model for planar ferrite growth in Fe-C-X alloys. *Metall. Mater. Trans. A* 44 (8), 3456–3471.
- Chen, H., van der Zwaag, S., 2014. A general mixed-mode model for the austenite-to-ferrite transformation kinetics in Fe-C-M alloys. *Acta Mater.* 72, 1–12.
- Chen, H., Zhu, B., Militzer, M., 2016. Phase field modeling of cyclic austenite-ferrite transformations in Fe-C-Mn alloys. *Metall. Mater. Trans. A* 47 (8), 3873–3881.
- Perevoshchikova, N., Appolaire, B., Teixeira, J., Aeby-Gautier, E., Denis, S., 2013. Investigation of the growth kinetics of $\gamma \rightarrow \alpha$ in Fe-C-X alloys with a thick interface model. *Comput. Mater. Sci.* 82, 151–158.
- Mathevon, A., Perez, M., Massardier, V., *et al.*, 2020. Gibbs energy minimization model for the austenite-ferrite phase transformation in Fe-C-X-Y alloys. *Phil. Mag. Lett.*
- Desgranges, C., Bertrand, N., Abbas, K., Monceau, D., Poquillon, D., 2004. Numerical model for oxide scale growth with explicit treatment of vacancy fluxes. *Mater. Sci. Forum* 461–464, 481–488.
- Bertrand, N., Desgranges, C., Gauvain, D., Monceau, D., Poquillon, D., 2004. Low temperature oxidation of pure iron: Growth kinetics and scale morphologies. *Mater. Sci. Forum* 461–464, 591–598.
- Dupin, N., Ansara, I., Servant, C., *et al.*, 1999. Thermodynamic database for zirconium alloys. *J. Nucl. Mater.* 275 (3), 287–295.
- Le Saux, M., Brachet, J.-C., Vandenberghe, V., *et al.*, 2011. Influence of pre-transient oxide on LOCA high temperature steam oxidation and post-quench mechanical properties of zircaloy-4 and M5™ cladding. In: *Proceedings of the 2011 Water Reactor Fuel Performance Meeting*, Chengdu, China.
- Brachet, J.-C., Vandenberghe, V., Portier, L., *et al.*, 2008. Hydrogen content, preoxidation, and cooling scenario effects on post-quench microstructure and mechanical properties of zircaloy-4 and m5 alloys in LOCA conditions. *J. ASTM Int.* 5 (5), 28.
- Toffolon-Masclat, C., Desgranges, C., Corvalan-Moya, C., Brachet, J.-C., 2011. Simulation of the $\beta \rightarrow \alpha(0)$ phase transformation due to oxygen diffusion during high temperature oxidation of zirconium alloys. *Solid State Phenom.* 172–174, 652–657.
- Chuto, T., Nagase, F., Fuketa, T., 2009. High temperature oxidation of Nb-containing Zr alloy cladding in LOCA conditions. *Nucl. Eng. Technol.* 41, 163–170.
- Guilbert, S., Lacote, P., Montigny, G., *et al.*, 2015. Effect of a pre-oxide on zircaloy-4 high temperature steam oxidation and post-quench mechanical properties. In: *Comstock, B., Barberis, P. (Eds.), Proceedings of the Zr in the Nuclear Industry*, vol. 17. West Conshohocken, PA: ASTM International, pp. 952–978.
- Mazères, B., Desgranges, C., Toffolon-Masclat, C., Monceau, D., 2016. Experimental study and numerical simulation of high temperature (1100–1250°C) oxidation of prior-oxidized zirconium alloy. *Corros. Sci.* 103, 10–19.
- Baek, J.H., Jeong, Y.H., 2007. Steam oxidation of Zr-1.5Nb-0.4Sn-0.2Fe-0.1Cr and zircaloy-4 at 900–1200°C. *J. Nucl. Mater.* 361 (1), 30–40.
- Perron, A., Toffolon-Masclat, C., Ledoux, X., *et al.*, 2014. Understanding sigma-phase precipitation in a stabilized austenitic stainless steel (316Nb) through complementary CALPHAD-based and experimental investigations. *Acta Mater.* 79, 16–29.

40. Chandra, K., Kain, Vivekanand., Bhutani, Vikas., *et al.*, 2012. Low temperature thermal aging of austenitic stainless steel welds: Kinetics and effects on mechanical properties. *Mater. Sci. Eng. A* 534, 163–175.
41. Morris, D., 1979. The influence of sigma phase on creep ductility in type 316 stainless steel. *Scr. Metall.* 13, 1195–1196.
42. May, V.E., 1985. Sigma-phase embrittlement of austenitic stainless-steel FCCU regenerator internals. *Mater. Perform.* 24 (12), 18–22.
43. Weiss, B., Stickler, R., 1972. Phase instabilities during high temperature exposure of 316 austenitic stainless steel. *Metall. Mater. Trans. B* 3, 851–866.
44. Mandiang, Y., Cizeron, G., 1996. Précipitation de la phase sigma dans un acier inoxydable du type 316 Ti contenant du phosphore (acier Z 6 CNDTP 17-13). *Revue de Métallurgie* 93, 619–628.
45. Sourmail, T., 2001. Precipitation in creep resistant austenitic stainless steels. *Mater. Sci. Technol.* 17, 1.
46. Gill, T.P.S., Gnanamoorthy, J.B., 1982. A method for quantitative analysis of delta-ferrite, sigma and M23C6 carbide phases in heat treated Type 316 stainless steel weldments. *J. Mater. Sci.* 17, 1513–1518.
47. Barcik, J., 1988. Mechanism of sigma-phase precipitation in Cr-Ni austenitic steels. *Mater. Sci. Technol.* 4 (1), 5–15.
48. Lee, T.-H., Oh, C.-S., Gil, C., Kim, S.-J., Takaki, S., 2004. Precipitation of sigma phase in high-nitrogen austenitic 18Cr–18Mn–2Mo–0.9N stainless steel during isothermal aging. *Scr. Mater.* 50, 1325–1328.
49. Lee, T.-H., Kim, S.-J., Takaki, S., 2006. Time-temperature-precipitation characteristics of high-nitrogen austenitic Fe-18Cr-18Mn-2Mo-0.9N steel. *Metall. Mater. Trans. A* 37A (December), 3445.
50. Badji, R., Bouabdallah, M., Bacroix, B., *et al.*, 2008. Effect of solution treatment temperature on the precipitation kinetic of sigma -phase in 2205 duplex stainless steel welds. *Mater. Sci. Eng. A* 496, 447–454.
51. Kozeschnik, E., 2013. *Modeling Solid-State Precipitation*. New York: Momentum Press, LLC.
52. Esmaili, S., Lloyd, D.J., Poole, W.J., 2003. A yield strength model for the Al-Mg-Si-Cu alloy AA6111. *Acta Mater.* 51, 2243–2257.
53. Clouet, E., Nastar, M., Sigli, C., 2004. Nucleation of {Al₃Zr} and {Al₃Sc} in aluminum alloys: From kinetic Monte-Carlo simulations to classical theory. *Phys. Rev. B* 69, 064109.
54. Clouet, E., Nastar, M., Barbu, A., Sigli, C., Martin, G., 2005. Precipitation in Al-Zr-Sc alloys: A comparison between kinetic Monte Carlo, cluster dynamics and classical nucleation theory. In: Howe, J.M., Laughlin, D.E., Lee, J.K., Srolovitz, D.J., Dahmen, U. (Eds.), *Solid-Solid Phase Transformations in Inorganic Materials*.
55. Russell, K.C., 1980. Nucleation in solids. In: Aaronson, H.I. (Ed.), *Phase Transformations*. American Society for Metals, pp. 219–268.
56. Perez, M., Dumont, M., Acevedo-Reyes, D., 2008. Implementation of the classical nucleation theory for precipitation. *Acta Mater.* 56, 2119–2132.
57. Perez, M., Dumont, M., Acevedo-Reyes, D., 2009. Corrigendum to "Implementation of the classical nucleation theory for precipitation". *Acta Mater.* 57, 1318.
58. Clouet, E., Barbu, A., Laé, L., Martin, G., 2005. Precipitation kinetics of Al₃Zr and Al₃Sc in aluminum alloys modeled with cluster dynamics. *Acta Mater.* 53 (8), 2313–2325.
59. Maugis, P., Soisson, F., Lae, L., 2005. Kinetics of precipitation: Comparison between monte carlo simulations, cluster dynamics and the classical theories. *Defect Diffus. Forum* 237–240, 671–676.
60. Perez, M., 2005. Gibbs-Thomson effect in phase transformations. *Scr. Mater.* 52 (8), 709–712.
61. Du, Q., Perez, M., Poole, W.J., Wells, M., 2012. Numerical integration of the Gibbs–Thomson equation for multicomponent systems. *Scr. Mater.* 66, 419–422.
62. Wagner, R., Kampmann, R., Voorhees, P.W., 2001. Homogeneous second-phase precipitation. In: Kosterz, G. (Ed.), *Phase Transformations in Materials*. John Wiley & Sons, Ltd, pp. 309–407.
63. Kozeschnik, E., Buchmayr, B., 2001. *MatCalc – A Simulation Tool for Multicomponent Thermodynamics, Diffusion and Phase Transformation Kinetics*. Graz University of Technology.
64. Kozeschnik, E., Svoboda, J., Fratzl, P., Fisher, F.D., 2004. Modelling of kinetics in multi-component multi-phase systems with spherical precipitates II: Numerical solution and application. *Mater. Sci. Eng. A* 385, 157–165.
65. Chen, Q., Wu, K., Sterner, G., Mason, P., 2014. Modeling precipitation kinetics during heat treatment with calphad-based tools. *J. Mater. Eng. Perform.* 23 (12), 4193–4196.
66. Sonderegger, B., Kozeschnik, E., 2009. Size dependence of the interfacial energy in the generalized nearest-neighbor broken-bond approach. *Scr. Mater.* 60 (8), 635–638.
67. Philibert, J., Vignes, A., Bréchet, Y., Combrade, P., 1998. *Métallurgie: Du minerai au matériau*. Elsevier-Masson.
68. Ratti, M., Leuvrey, D., Mathon, M.H., de Carlan, Y., 2009. Influence of titanium on nano-cluster (Y, Ti, O) stability in ODS ferritic materials. *J. Nucl. Mater.* 386–388, 540–543.
69. Giusca, D., Popescu, I., 1939. *Bull. Soc. Roum. Phys.* 40, 18.
70. Mumme, W.G., Wadsley, A.D., 1968. The structure of orthorhombic Y₂TiO₅, An example of mixed seven- and five fold coordination. *Acta Crystallogr.* B24, 1327–1333.
71. Chinnappan, R., 2014. Thermodynamic stability of oxide phases of Fe–Cr based ODS steels via quantum mechanical calculations. *Calphad* 45, 188–193.
72. Hirata, A., Fujita, T., Wen, Y.R., *et al.*, 2011. Atomic structure of nanoclusters in oxide-dispersion strengthened steels. *Nat. Mater.* 10, 922–926.
73. Ribis, J., de Carlan, Y., 2012. Interfacial strained structure and orientation relationships of the nanosized oxide particles deduced from elasticity-driven morphology in oxide dispersion strengthened materials. *Acta Mater.* 60 (1), 238–252.
74. Brocq, M., Radiguet, B., Le Breton, J.-M., *et al.*, 2010. Nanoscale characterisation and clustering mechanism in an Fe–Y₂O₃ model ODS alloy processed by reactive ball milling and annealing. *Acta Mater.* 58 (5), 1806–1814.
75. Laurent-Brocq, M., Legendre, F., Mathon, M.-H., *et al.*, 2012. Influence of ball-milling and annealing conditions on nanocluster characteristics in oxide dispersion strengthened steels. *Acta Mater.* 60 (20), 7150–7159.
76. Williams, C.A., Unifantowicz, P., Baluc, N., Smith, G.D.W., Marquis, E.A., 2013. The formation and evolution of oxide particles in oxide-dispersion-strengthened ferritic steels during processing. *Acta Mater.* 61 (6), 2219–2235.
77. Wu, Y., Haney, E.M., Cunningham, N.J., Odette, G.R., 2012. Transmission electron microscopy characterization of the nanostructures in nanostructured ferritic alloy MA957. *Acta Mater.* 60 (8), 3456–3468.
78. Hirata, A., Fujita, T., Liu, C.T., Chen, M.W., 2012. Characterization of oxide nanoprecipitates in an oxide dispersion strengthened 14YWT steel using aberration-corrected STEM. *Acta Mater.* 60 (16), 5686–5696.
79. Hin, C., Wirth, B.D., Neaton, J.B., 2009. Formation of Y₂O₃ nanoclusters in nanostructured ferritic alloys during isothermal and anisothermal heat treatment: A kinetic Monte Carlo study. *Phys. Rev. B* 80, 134118.
80. Boulnat, X., Perez, M., Fabrégue, D., Cazottes, S., de Carlan, Y., 2016. Characterization and modeling of oxides precipitation in ferritic steels during fast non-isothermal consolidation. *Acta Mater.* 107, 390–403.
81. Alinger, M.J., 2004. *On the Formation and Stability of Nanometer Scale Precipitates in Ferritic Alloys During Processing and High Temperature Service*. PhD Thesis. Santa Barbara: University of California.
82. Boulnat, X., Perez, M., Fabrégue, D., *et al.*, 2014. Microstructure evolution in nano-reinforced ferritic steel processed by mechanical alloying and spark plasma sintering. *Metall. Mater. Trans. A* 45A, 1485–1497.
83. Perez, M., Dumont, M., Acevedo-Reyes, D., 2009. Corrigendum to "Implementation of classical nucleation and growth theories for precipitation". *Acta Mater.* 57 (4), 1318.
84. Perez, M., Dumont, M., Acevedo-Reyes, D., 2008. Implementation of classical nucleation and growth theories for precipitation. *Acta Mater.* 56 (9), 2119–2132.
85. Perez, M., 2007. *Approche multi-échelle de la précipitation*. Habilitation à diriger des recherches.
86. Salles, N., Boulnat, X., Borbély, A., *et al.*, 2015. In situ characterization of microstructural instabilities: Recovery, recrystallization and abnormal growth in nanoreinforced steel powder. *Acta Mater.* 87, 377–389.

87. Hin, C., Wirth, B.D., 2011. Formation of oxide nanoclusters in nanostructured ferritic alloys during anisothermal heat treatment: A kinetic monte carlo study. *Mater. Sci. Eng. A* 528 (4–5), 2056–2061.
88. Klugkist, P., Herzig, C., 1995. Tracer diffusion of titanium in α -iron. *Phys. Status Solidi* 148, 413–421.
89. Barlow, R., Grundy, P.J., 1969. The determination of the diffusion constants of oxygen in nickel and α -iron by an internal oxidation method. *J. Mater. Sci.* 4, 797–801.
90. Takada, J., Adachi, M., 1986. Determination of diffusion coefficient of oxygen in α -iron from internal oxidation measurements in Fe-Si alloys. *J. Mater. Sci.* 21, 2133–2137.
91. Barnard, L., Odette, G.R., Szlufarska, I., Morgan, D., 2012. An ab initio study of Ti–Y–O nanocluster energetics in nanostructured ferritic alloys. *Acta Mater.* 60 (3), 935–947.
92. Murali, D., Panigrahi, B.K., Valsakumar, M.C., Sundar, C.S., 2011. Diffusion of Y and Ti/Zr in bcc iron: A first principles study. *J. Nucl. Mater.* 419 (1–3), 208–212.
93. Ratti, M., 2010. Development of new ferritic/martensitic steels for RNR-Na tube cladding materials, translated from 'Développement de nouvelles nuances d'aciers ferritiques/martensitiques pour le gainage d'éléments combustibles des Réacteurs à Neutrons Rapides au sodium' PhD Thesis. Institut Polytechnique de Grenoble.
94. Miller, M.K., Hoelzer, D.T., Kenik, E.A., Russell, K.F., 2004. Nanometer scale precipitation in ferritic MA/ODS alloy MA957. *J. Nucl. Mater.* 329–333 (Part A), 338–341.
95. de Castro, V., Marquis, E.A., Lozano-Perez, S., Pareja, R., Jenkins, M.L., 2011. Stability of nanoscale secondary phases in an oxide dispersion strengthened Fe–12Cr alloy. *Acta Mater.* 59 (10), 3927–3936.
96. Salez, N., Donnadieu, P., Courtois-Manara, E., *et al.*, 2020. On morphological anisotropy and local texture in a ferritic ODS steel: From as-milled powder to consolidated states. *Mater. Charact.* (In preparation).
97. Zhang, C., Enomoto, M., Yamashita, T., Sano, N., 2004. Cu precipitation in a prestrained Fe1.5 wt pct Cu alloy during isothermal aging. *Metall. Mater. Trans. A* 35, 1262–1272.
98. Perez, M., Perrard, F., Massardier, V., *et al.*, 2005. Low temperature solubility of copper in iron: Experimental study using thermoelectric power, small angle X-ray scattering and tomographic atom probe. *Philos. Mag.* 85 (20), 2197–2210.
99. Deschamps, A., Nicolas, M., Perrard, F., Bley, F., 2005. Non-isothermal precipitation kinetics in metallic alloys. In: *Solid to solid Phase Transformations In Inorganic Materials*. Scientific.Net.
100. Soisson, F., Fu, C.-C., 2007. Cu-precipitation kinetics in α -Fe from atomistic simulations: Vacancy-trapping effects and cu-cluster mobility. *Phys. Rev. B* 76 (21), 214102
101. Jourdan, T., Soisson, F., Clouet, E., Barbu, A., 2010. Influence of cluster mobility on Cu precipitation in α -Fe: A cluster dynamics modeling. *Acta Mater.* 58 (9), 3400–3405.
102. Stechauner, G., Kozeschnik, E., 2015. Thermo-kinetic modeling of Cu precipitation in α -Fe. *Acta Mater.* 100, 135–146.
103. Dépinoy, S., Menut, D., Toffolon-Masclat, C., *et al.*, 2015. Evolution of microstructure during tempering and its influence on the mechanical behavior of 2.25Cr-1Mo bainitic steel. In: *Proceedings of the International Conference on Solid-Solid Phase Transformations in Inorganic Materials*, PTM 2015.
104. Murakami, Y., Nomura, T., Watanabe, J., 1982. Application of 21/4Cr-1Mo Steel for Thick-Wall Pressure Vessels. Denver: ASTM, pp. 383–417.
105. Blagoeva, D.T., Debarberis, L., Jong, M., Pierick, P., 2014. Stability of ferritic steel to higher doses: Survey of reactor pressure vessel steel data and comparison with candidate materials for future nuclear systems. *Int. J. Press. Vessel. Pip.* 122, 1–5.
106. Baker, R.G., Nutting, J., 1959. The tempering of 2.25%Cr-1%Mo steel after quenching and normalizing. *J. Iron Steel Inst.* 7, 257–258.
107. Zajac, S., Komenda, J., Morris, P., *et al.*, 2005. Quantitative Structure-Property Relationships for Complex Bainitic Microstructures. Report EUR21245EN. Technical report, Technical Steel Research. European Commission.
108. Choo, J., Kang, Y.H., Pyun, S.I., Urbanic, V.F., 1994. Effect of composition and heat treatment on the microstructure and corrosion behavior of Zr-Nb alloys. *J. Nucl. Mater.* 209, 226–235.
109. Toffolon, C., Brachet, J.-C., Guilbert, T., *et al.*, 2001. Vieillessement thermique des alliages de zirconium-niobium en phase alpha (570°C). *J. Phys. IV* 11. (1–99 – 1–108).